



Full length article

Pitting resistance of reduced graphene oxide-layered double hydroxide reinforced aluminum composite coating deposited by cold spraying



Gengzhe Shen^a, Liuyan Zhang^{a,*}, Huishu Wu^d, Zhiwei Gu^{a,c}, Shixuan Wang^a, Yuwen Liu^a, Qiongbin Zheng^a, Guibin Tan^b, Xiaohua Jie^a

^a School of Materials and Energy, Guangdong University of Technology, Guangzhou 510006, PR China

^b State Key Laboratory of Precision Electronic Manufacturing Technology and Equipment, Guangdong University of Technology, Guangzhou 510006, PR China

^c State Key Laboratory of Tribology, Tsinghua University, Beijing 100084, PR China

^d Materials Science and Engineering, Dongguan University of Technology, Dongguan 523808, PR China

ARTICLE INFO

ABSTRACT

Keywords:

Magnesium alloys
Low-pressure cold spray
Reduced graphene oxide
Layered double hydroxides
Corrosion resistance

Cold spraying aluminum-based coatings are widely used for corrosion protection of metals such as steel and magnesium alloy. However, poor pitting resistance and short protection life are the shackles of aluminum-based coating. In order to solve this problem, this paper innovatively utilized the synergistic effect of reduced graphene oxide (rGO) and layered double hydroxide (LDH) to modify the coating efficiently. Al-GLG coatings were prepared by cold spraying rGO and LDH-modified aluminum powders. The structure, composition and corrosion resistance of the Al-GLG coating were analyzed and compared with that of unmodified Al-based coating and graphene-modified Al-based (Al-G) coating. As a result, the Al-GLG coating presents a continuous network GLG surrounding the deformed aluminum powder, and this special coating exhibits pitting resistance and long life. The corrosion current density of the Al-GLG coating is only $0.01287 \mu\text{A}\cdot\text{cm}^{-2}$, which is three orders of magnitude lower than that of the Al-based coating, and its pitting potential is about $-0.24 \text{ V}_{\text{SCE}}$, which is over 540 mV higher than that of the Al-based coating. During the full immersion test, the Al-GLG coating keeps the largest R_{c} ($7.21 \times 10^4 \Omega\cdot\text{cm}^2$) and low-frequency impedance modulus $|Z|_{0.01\text{Hz}}$ ($3.66 \times 10^4 \Omega\cdot\text{cm}^2$). The corrosion resistance mechanism of the Al-GLG coating was investigated via field emission scanning electron microscope (FE-SEM), X-ray diffraction (XRD), Raman and X-ray photoelectron spectroscopy (XPS), respectively. The excellent pitting corrosion resistance of the Al-GLG coating is attributed to the synergistic effect of the shielding effect of reduced graphene oxide and the ion exchange inhibition effect of LDH.

1. Introduction

Magnesium alloy is a structurally stable and lightweight material. It has broad prospects in engineering applications such as the aerospace and automobile industry [1–4]. However, the high chemical activity and poor corrosion resistance limit the wide industrial applications of Mg alloys. Aluminum-based coatings have the advantage of stability, high efficiency, great potential in corrosion and friction resistance, and so on [5,6]. So aluminum-based coatings have become the focus of research in the anti-corrosion of magnesium alloys. Aluminum-based coatings can prepare on the surface of magnesium alloys through surface modification, such as electroplating [7], thermal spraying [5], vapor deposition [8], and so on. However, experimental conditions often limit these technologies, leading to the expensive cost of coatings preparation, low

protection efficiency, and severe defects. Therefore, developing a technology that is easy to prepare coatings, low cost, and efficient is still a hot spot in current research.

Low-pressure cold spraying (LPCS) is a new type of surface coating preparation technology, which forms protection by accelerating micron metal powder (5–50 μm) to supersonic speed (500–1200 m/s) and depositing it on the surface of the substrate [9,10]. LPCS is efficient and easy to prepare aluminum-based coatings on magnesium alloy surfaces [11,12]. However, the aluminum-based coatings prepared by LPCS show some severe defects [6,12,13], which cause the aluminum-based coatings to be prone to pitting corrosion in 3.5 wt% NaCl solution. Therefore, how to improve the corrosion resistance of aluminum-based coatings, slow down pitting corrosion, and prolong coating life is still the focus of current research.

* Corresponding author.

E-mail address: zlyjust@gdut.edu.cn (L. Zhang).

Thus, numerous researches have been dedicated to improving the anti-corrosion performance of metal-based coating by compounding various nanomaterials [14–16]. In recent years, Graphene oxide (GO) has been widely used as an essential role in improving the corrosion resistance of metal-based coatings [17,18]. Graphene oxide (GO) has defects such as oxygen-containing functional groups (-OH, -COOH) on the surface of graphene [19–21]. It owns excellent performance of impermeability and mechanical properties. Jyotheender et al. used electrodeposition to prepare a Ni-GO composite coating on a low-carbon steel substrate. Due to the impermeability of GO, the Ni-GO coating had the lowest corrosion rate [22]. Rekha et al. prepared zinc (Zn) and GO composite coatings with different microstructures. GO promoted the reduction of the electrodeposited Zn grain size, which was conducive to forming the passivation film and building Zn-GO-Zn multilayer coating. The introduction of GO significantly improved the anti-corrosion performance of zinc-based coatings [23].

In recent years, layered double hydroxide (LDH) in metal corrosion has attracted much attention. The molecular formula of LDH is $[M_1^{2+} \cdot M_x^{3+}(\text{OH})_2]_x^+ \cdot (\text{A}_m^-)_x \cdot n\text{H}_2\text{O}$, where M^{2+} and M^{3+} represent two valence metal cations (for example, Mg^{2+} , Cu^{2+} , Zn^{2+}) and trivalent Metal cations (for example, Al^{3+} , Fe^{3+} , Co^{3+}). A_m^- is the interlayer anion (such as NO_3^- , Cl^- , CO_3^{2-}), and m is the charge of the interlayer anion [24–26]. On the one hand, the unique layered structure of LDH provides absorption of corrosive ions and inhibits the corrosive effect of corrosive ions. On the other hand, the unique layered structure provides a barrier layer with high ionic resistivity to prevent the penetration of corrosive agents. Gao et al. prepared rGO/ZnAl-LDH film on the surface of Magnesium alloys by one-step in situ synthesis [26]. It found that rGO/ZnAl-LDH film greatly improved the corrosion resistance of magnesium alloys. Wu et al. fabricated A magnesium-aluminum layered double-hydroxides (MgAl-LDHs) coating by hydrothermal on the surface of Mg alloy, and then electrophoretic deposition of an Al_2O_3 layer. It improved the corrosion resistance mechanisms of magnesium alloy coatings [27]. Zhang et al. prepared pre-spraying aluminum coating with rGO. The MgAl-LDH was prepared by a hydrothermal method on the surface of the aluminum coating with rGO, and the corrosion resistance of the Mg alloy was improved [28]. The method of in situ growth of LDH composite coatings on the surface of metal alloys or coatings has been widely used [21,29–31]. However, the anti-corrosion coatings prepared by this method are a two-dimensional plane structure, which has disadvantages such as easy detachment, weak permeability resistance, and rapid failure during the soaking process. Since no shielding network is formed in the three-dimensional (3D) space, the corrosion rate rapidly accelerates after failure. And once the corrosive medium penetrates the anti-corrosion coatings, it will directly corrode the substrate itself.

However, it is difficult to fill LDH into aluminum-based coatings to form a three-dimensional anti-corrosion network and improve anti-corrosion performance. It is mainly because LDH flakes tend to stack or even agglomerate in applications, and it is difficult to disperse and poorly compatible with metal powders [32,33]. The metal powder compounded with LDH has poor fluidity during cold spraying. Inspired by the literature, Wen et al. prepared LDH on the surface of rGO via a one-step process, and then rGO-LDH as micro-nano fillers into a waterborne epoxy (EP). The rGO-LDH has good dispersibility and stability [34]. Hu et al. verified that the rGO-LDH has an excellent synergistic effect between rGO and LDH layers [35]. In our previous study, Zhang et al. successfully improved the corrosion resistance of Zn/Al-based coatings with rGO. It used the in-situ reduction method to reduce GO to rGO coated on the surface of Zn/Al powders and fill the interior of the Zn/Al-based coating with rGO uniformly [6,36].

Herein, we proposed a simple and effective strategy to introduce LDH and rGO into aluminum-based coatings, which can enhance the surface protection of Mg alloys. Zinc aluminum-layered double hydroxide (ZnAl-LDH) was in situ grown on the surface of GO by hydrothermal method to obtain rGO-LDH. GO and rGO-LDH attracted each

other, which were reduced and assembled to form rGO-LDH-rGO (GLG) on the surface of aluminum powder. This way realized the dispersion and compatibility of rGO and LDH on the surface of aluminum powder. Aluminum powder modified by GLG was deposited on the magnesium alloy by low-pressure cold spraying to form a protective Al-GLG coating. Both rGO and ZnAl-LDH formed a 3D continuous anti-corrosion network surrounding the deformed aluminum powder. Under the synergistic effect of rGO and ZnAl-LDH, Al-GLG coating will have shielding corrosion inhibition for corrosive media. Benefiting from these merits, the Al-GLG coating will exhibit excellent pitting corrosion resistance and long life in the anti-corrosion process of magnesium alloys.

2. Experimental method

2.1. Materials

In this experiment, AZ31B Mg alloy with a size of $15\text{ mm} \times 15\text{ mm} \times 3\text{ mm}$ was selected as the matrix. After polishing with 400, 600, and 800-mesh sandpaper, it was sandblasted and roughened to $\text{R}_s \sim 5\text{ }\mu\text{m}$, then ultrasonically cleaned, air-dried, and cold sprayed to prepare samples. It used spherical Al powder ($35\text{--}45\text{ }\mu\text{m}$, purity $\geq 99\%$) and Al_2O_3 powder ($40\text{--}50\text{ }\mu\text{m}$, purity $\geq 99\%$), purchased from Xinrongyuan Industrial Co., Ltd. Aluminum nitrate nonahydrate ($\text{Al}(\text{NO}_3)_3 \cdot 9(\text{H}_2\text{O})$), zincnitrate hexahydrate ($\text{Zn}(\text{NO}_3)_2 \cdot 6(\text{H}_2\text{O})$), and ammonium hydroxide were purchased at Shanghai aladdin biochemical technology Co., Ltd. According to our previous research, GO was prepared by the Hummers method after an improved test scheme, and the GO characterization was completed simultaneously.

2.2. Preparation of Al-GLG composite coating

The previous literature had reported the method of coating aluminum powder with graphene oxide; when the graphene oxide content was 0.2 wt%, the resulting cold spray coating had the best anti-corrosion performance [6]. The rGO-ZnAl-LDH composite material was synthesized by the hydrothermal method. Firstly, 100 ml of the GO suspension solution with a concentration of 0.2 mg/ml was taken, and added 0.9378 g of $\text{Al}(\text{NO}_3)_3 \cdot 9(\text{H}_2\text{O})$ and 1.4875 g of $\text{Zn}(\text{NO}_3)_2 \cdot 6(\text{H}_2\text{O})$. The mixed solution was dispersed by ultrasonic stirring for 60 min. Ammonia water was added to the solution to adjust the pH value to 8, and then it was placed in the hydrothermal reaction kettle to maintain the temperature at 90°C and react for 24 h. GO was reduced to reduced graphene oxide (rGO) in this reaction [34]. After the reaction, 3500 rpm/min was centrifuged and washed to $\text{pH} = 7.0$. ZnAl-LDH was grown in situ on the surface of rGO. It was marked as rGO-LDH.

Then it took 100 ml of the GO suspension solution with a 0.2 mg/ml concentration. The graphene oxide was well dispersed in the deionized water by ultrasound and stirred for 30 min, then 20 g of pure spherical aluminum powder was added to the hybrid solution of the rGO-LDH and stirred for 5 min, then added GO solution. GO was used as a carrier to connect rGO-LDH and aluminum powder. GO was reduced by aluminum powder [37]. Finally, the surface of aluminum powder was coated by rGO-LDH and rGO; the composite materials rGO-LDH and rGO as a unit were marked as rGO-LDH-rGO (GLG). Al-GLG powder was obtained after washing and vacuum drying.

20 g Al-GLG powder was weighed and mixed with 5 g Al_2O_3 powder to prepare pre-sprayed powder. The compressed air was 600°C , the pressure was 0.65 MPa, and the nozzle gun moving speed was 150 mm/s. The powder supply rate was 0.3 g/s, and the coating obtained was recorded as Al-GLG after cold spraying. Used the same method to prepare Al-G and Al coatings as a comparison sample. The Al, Al-G and Al-GLG coatings were abraded with emery papers up to 2000 grits, and their thickness were kept in the range of 200–300 μm . As shown in Fig. S1, the thickness of the compared coatings were similar in the work.

The overall technical route of Al-GLG coating preparation is briefly illustrated in Fig. 1. The Al-GLG coating was formed on the surface of Mg

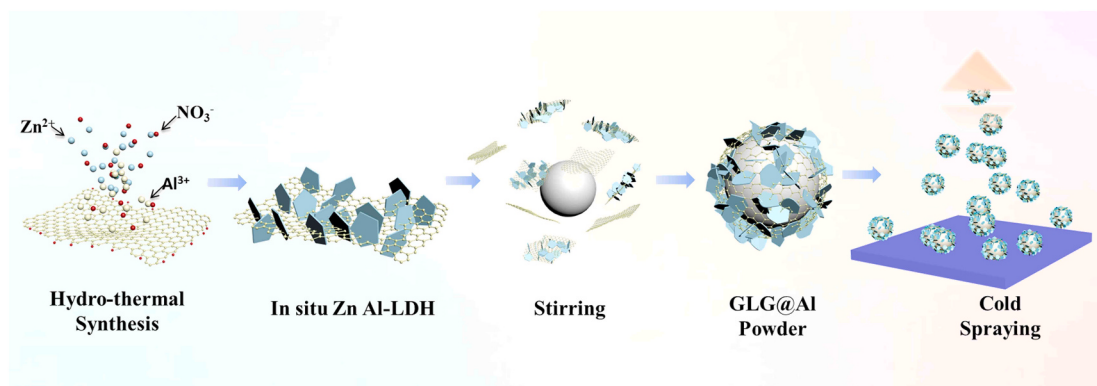


Fig. 1. Technical route scheme of cold spraying Al-GLG coating on Mg alloy.

alloy by LPCS.

2.3. Characterization

The morphology of GO, rGO-LDH, Al-GLG coating, Al-G coating, Al coating, Mg, and the corresponding corrosion production was observed by field emission scanning electron microscope (FE-SEM, Hitachi S-4800) Morphology. A scanning electron microscope (SEM, SU8010) and 3D laser measuring microscope (OLS4000, Olympus) were used to observe the etched cross-sections of Al-GLG coating, Al-G coating, Al coating, Mg, etc. X-ray diffractometer (D/MAX Ultima IV; Rigaku Co., Japan) was used to detect the phase of rGO-LDH, GO, ZnAl-LDH, different coatings, and corresponding corrosion products. Raman spectroscopy (Model Laboratory RAM HR800, Raman) was used to analyze ZnAl-LDH and rGO-LDH. The rGO-LDH was detected by X-ray photo-electron spectroscopy (XPS; Thermo Fisher 250Xi, US) with Al Ka radiation (1486.6 eV). The morphology of the rGO-LDH was characterized by TEM (FEI Talos F200X). The surface electronegativity of GO, rGO-LDH and rGO-LDH-GO were measured by Zeta potential (Malvern Zetasizer Nano ZS90, Britain). The functional groups of Al-GLG powder were analyzed by Fourier transform infrared (FTIR, Nicolet iN10) at the wave number range of 400–4000 cm⁻¹. The pulling testing was tested by a push-pull force gauge (LE, LiShi, China).

In order to explore the electrochemical performance of the corrosion resistance of the samples, an electrochemical workstation (CHI660E, Shanghai; Chenhua Instrument Co., Ltd., China) was used to conduct an electrochemical corrosion resistance test on the samples. At room temperature 25 °C, the samples were placed in 3.5 wt% NaCl for electrochemical impedance spectroscopy (EIS) and potential dynamic polarization (PDP) curve tests. The samples were reserved an area of 1 cm × 1 cm as the working electrode, forming a three-electrode system with the auxiliary (platinum) and the reference electrode (saturated calomel electrode). Before monitoring, all samples were soaked for 30 min to obtain a stable open circuit potential.

In the PDP curve test, the potential was scanned from 250 mV below the open-circuit potential to 350 mV above the open-circuit potential at a scan rate of 1 mV/s. The electrochemical impedance spectra (EIS) curves of composite coatings, such as Mg, Al, Al-G, Al-GLG, etc., were measured after soaking for 24 h, 120 h, 240 h and 360 h. The EIS test frequency range was from 10⁵ Hz to 10⁻² Hz, with a sine signal disturbance with an amplitude of 10 mV. All curves were measured at the actual open circuit potential. Used the experimental impedance diagram ZsimpWin software to fit the corresponding equivalent circuit. After the immersion test, it was observed that the morphology of the corrosion product and the sample with an optical microscope and FE-SEM. XRD detected the phase of the corrosion product. The electrolyte potential on the surface of magnesium alloy and aluminum-based coating were analyzed by the software Comsol.

2.4. First-principles calculations

It performed the first-principles calculations in the framework of density functional theory (DFT) with the Vienna ab initio simulation package (VASP) [38]. The exchange-correlation energy was described by the Perdew-Burke-Ernzerhof (PBE) form of generalized-gradient approximation (GGA) exchange-correlation energy functional [38,39], in combination with the DFT-D3 correction [40]. The structure optimizations of rGO-LDH and rGO-LDH-rGO heterojunctions were carried out by allowing all atomic positions to vary and fixing lattice parameters until the energy difference of successive atom configurations was <10⁻⁴ eV. The force on each atom in the relaxed structures was <0.015 eV/Å. The cutoff energy for the plane-wave basis set was set to 400 eV. The k-point spacing was set to be smaller than 0.03 Å⁻¹ over the Brillouin Zone (BZ) [41].

3. Results and discussion

The schematic diagram of the micromorphology of GO and rGO-LDH are presented in Fig. 2a. An SEM image of the GO film is in Fig. 2b. GO has a typical wrinkled structure [13]. Inset plots show the Raman spectrum of GO and can be seen the characteristic peaks of "D" (1324 cm⁻¹) and "G" peaks (1583 cm⁻¹) [13,42]. SEM images of rGO-LDH from low to high magnifications are shown in Fig. 2c–e. It can be observed that the fold structure of reduced GO (rGO) has nanosheets. This phenomenon proves successful in situ growth of ZnAl-LDH onto the rGO surface [34]. Functional groups (−OH, −COOH) on the surface of GO act as nucleation sites inducing the in situ growth of ZnAl-LDH [43]. So ZnAl-LDH is staggered on the surface of rGO (Fig. 2e). The inset of Fig. 2c is the Raman spectrum of rGO-LDH, showing typical "M—O (538.65 cm⁻¹)", "NO₃ (1047.44 cm⁻¹)", "D (1322.44 cm⁻¹)" and "G (1602.07 cm⁻¹)" peak [13]. The EDS mapping of rGO-LDH is shown in Fig. 2f. The main elements are C, N, Zn, Al, and O, corresponding to rGO and ZnAl-LDH.

In order to demonstrate that ZnAl-LDH is successfully synthesized by in situ growing on the GO surface, GO, ZnAl-LDH, and rGO-LDH are investigated by XRD, respectively. As shown in Fig. 3a, the characteristic diffraction peak of graphene oxide is located at 2θ = 10.28° (002); this illustrates that oxygen-containing functional groups (−OH, −COOH) are on the surface of GO [34]. Moreover, the typical characteristic XRD peaks of ZnAl-LDH are located at 2θ = 10.42°, 20.20°, 31.54°, 59.82°, 61.18°, corresponding to (003), (006), (012), (010) and (113) respectively [34,44]. This XRD pattern of ZnAl-LDH and rGO-LDH have all the characteristic diffractions of ZnAl-LDH (JCPDS card No.48-1023), as shown in Fig. S2. In the XRD pattern, the typical characteristic XRD peaks of rGO-LDH are the same as ZnAl-LDH, but the XPS spectrum can confirm that rGO-LDH contains reduced graphene oxide. XPS is applied to determine the interactions between rGO and ZnAl-LDH further. As shown in Fig. 3b–f, XPS analysis full survey scans XPS spectrum of rGO-

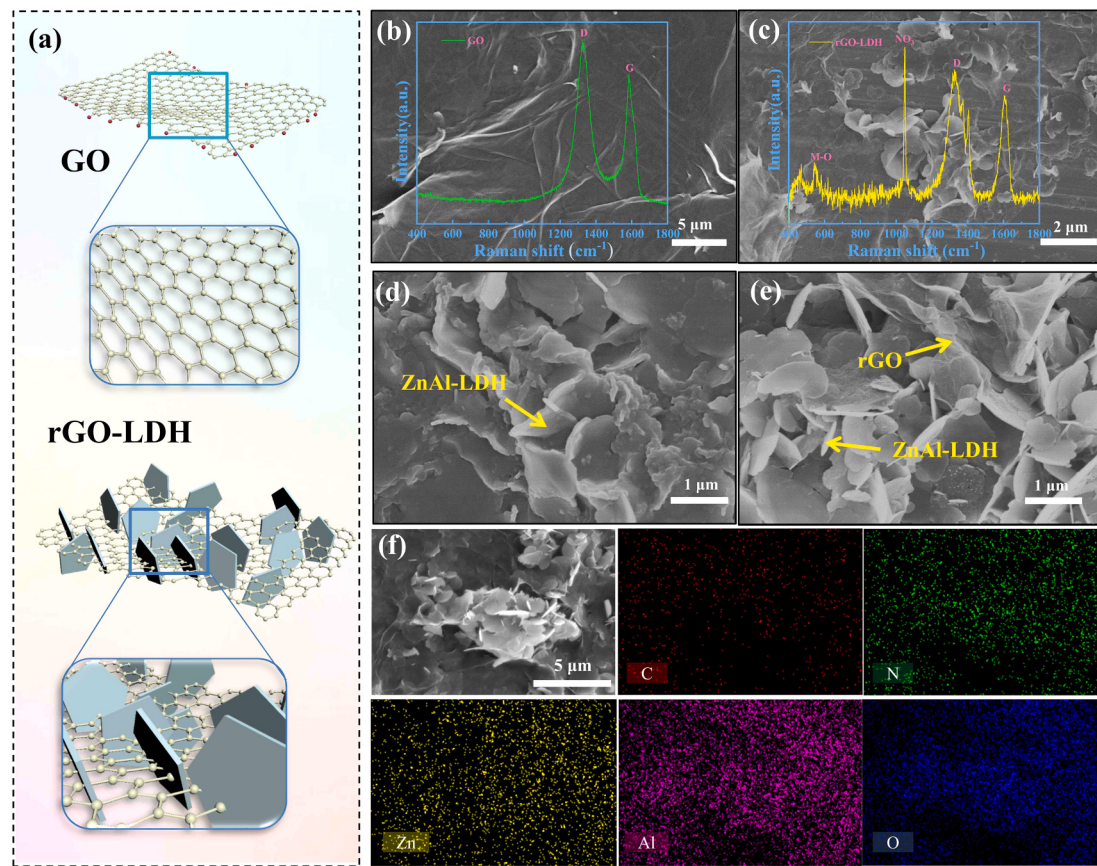
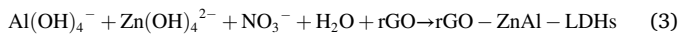


Fig. 2. (a) Schematic diagram of the micromorphology of GO and rGO-LDH; (b) SEM image of GO film, inset plots of the Raman spectrum of GO; (c–e) SEM image of rGO-LDH, inset plots of the Raman spectrum of rGO-LDH; (f) SEM image of rGO-LDH and corresponding C, N, Zn, Al, and O element mapping.

LDH, and its narrow scan XPS spectra of C 1s, O 1s, Zn 2p, Al 2p. XPS spectra of C 1s are shown in Fig. 3c, sp2 graphitized carbon as the dominant peak is acquired at 284.3 eV. The other four weak characteristic peaks in the XPS C1s spectra are located at 285.6 eV (−C—OH), 286.5 eV (C—O—C), 288.3 eV (C=O), and 290.1 eV (O—C=O), which can prove the existence of reduced graphene oxide [42,45]. O 1s is composed of three prominent peaks, as shown in Fig. 4d. The oxygen in the metallic hydroxide owns a characteristic peak at 530.4 eV, and the characteristic peak at 531.6 eV represents the C=O bond stretching vibration. These results confirm the presence of oxygen in the formed metallic hydroxide and reveal the nucleation of ZnAl-LDH nanosheets on the rGO surface, which are bonded to each other by the C=O bonds [29,46]. The water molecules on rGO-LDH correspond to the absorption peak at 532.4 eV [46,47]. In addition, the three prominent peaks at 1021.33 eV, 1044.43 eV, and 74.08 eV correspond to Zn2p 3/2, Zn2p 1/2, and Al 2p (Fig. 4e, f) [42,46], which confirms the binding of ZnAl-LDH on the surface of rGO. After discussing the results of XRD and XPS, the reaction schematic diagram can be described in Fig. 3g, and the corresponding reaction mechanism is as follows [48,49].



The inter-adsorbed stacked structure of rGO and ZnAl-LDH are confirmed by TEM images in Fig. 4a–d, the morphology of rGO-LDH (Fig. 4a) with irregular and fold nanosheets. ZnAl-LDH shows hexagonal layers and disintegrated morphology with many wrinkled sheets on its surface in Fig. 4b; these wrinkled sheets are rGO (Fig. 4c and d) [34].

This result indicates that rGO and ZnAl-LDH are interlaced with each other. The HRTEM image of rGO-LDH is shown in Fig. 4e, and the lattice between the adjacent fringes of the sample can be seen. It can be seen that the carbon hexagon and the corresponding FFT are the typical diffraction spots of graphene. The parallelogram of the hydrotalcite can be observed, and the corresponding FFT is the diffraction spots of ZnAl-LDH. It measured the interlayer spacing to be $d = 0.26$ nm, corresponding to the (012) peak of ZnAl-LDH [29,47].

To intuitively observe the interfacial binding interaction between rGO and ZnAl-LDH, the charge density differences (CDD) of the rGO-LDH system are calculated according to

$$\Delta\rho = \rho_{\text{rGO-LDH}} - \rho_{\text{rGO}} - \rho_{\text{LDH}} \quad (4)$$

where, $\rho_{\text{rGO-LDH}}$ is the charge density of the interfacial system and ρ_{rGO} and ρ_{LDH} are the charge densities of two partial surfaces. The CDD is displayed in Fig. 4g. To simplify the highly complex system of rGO-LDH, a model of the rGO-LDH system only consists of one layer of ZnAl-LDH layer and rGO (Fig. 4f), adopted to obtain a convergent result. The charge redistribution the interface exists in the interface. According to the simulation results, a strong interaction is excited between the ZnAl-LDH layer and rGO. A strong charge accumulation region appears below the ZnAl-LDH layer, near the O atoms and surrounding metal atoms (facing the rGO layer), and a charge depletion region above rGO, near the C atoms. This indicates strong electrostatic interaction between the ZnAl-LDH layer and rGO, building a strong binding force between the ZnAl-LDH layer and rGO. It is consistent with XPS results. Between the O atoms of ZnAl-LDH and the C atoms of rGO exist C=O bond stretching vibration, which corresponds to a characteristic peak at 531.6 eV [29,46]. And the structure of the rGO-LDH system is stable (Fig. 4g). Fig. 4h and i. rGO-LDH system display enhanced and continuous DOS

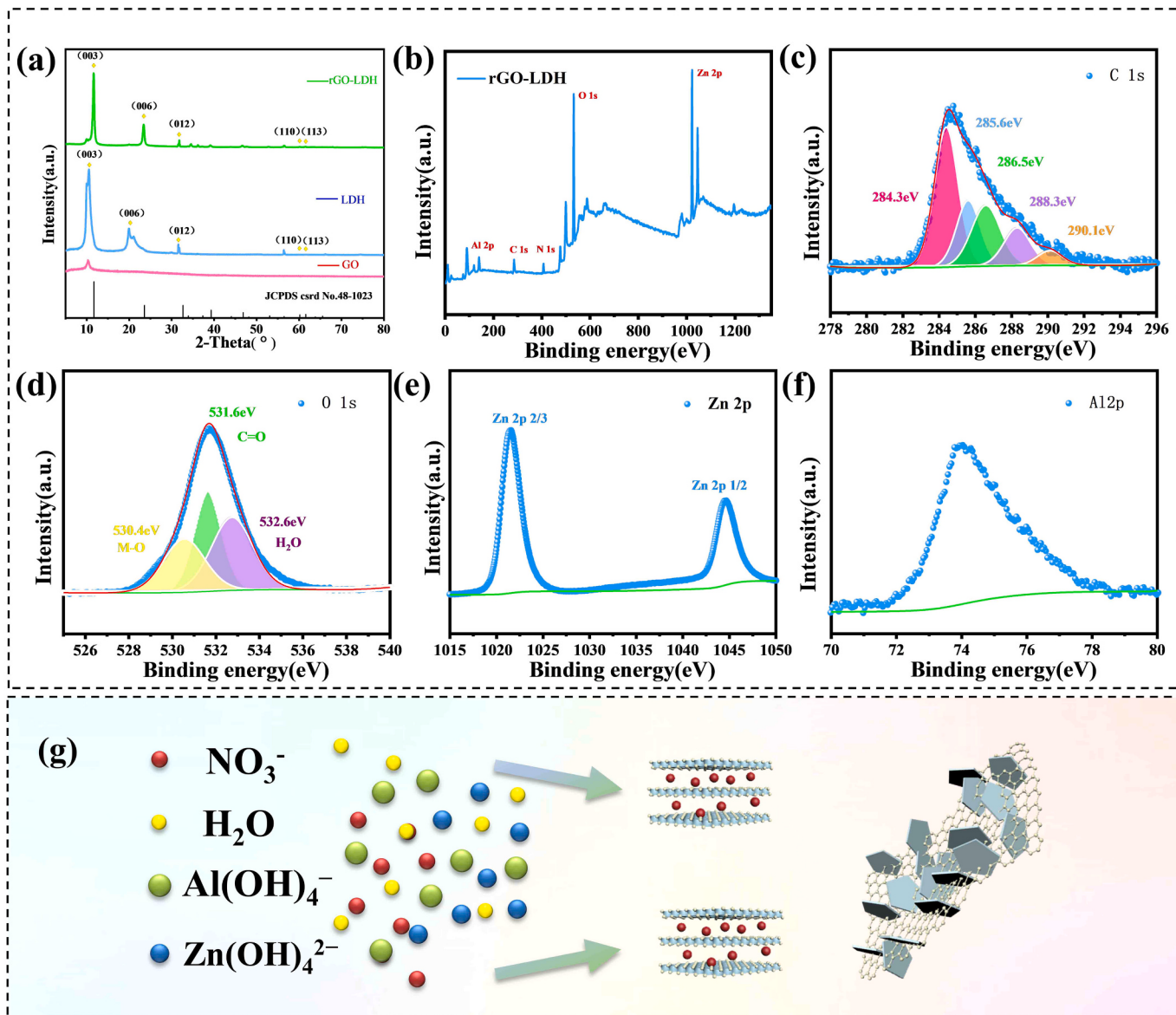


Fig. 3. (a) XRD analysis of GO, ZnAl-LDH, rGO-LDH; XPS spectra of rGO-LDH: (b) Survey scan; (c-f) narrow scan XPS spectrum of C 1s, O 1s, Zn 2p, Al 2p; (g) Schematic diagram of the synthesis of rGO-LDH.

around the Fermi region, illustrating that after the ZnAl-LDH layer and rGO form an integral, the rGO-LDH system owns a good electron transfer.

A schematic diagram of the GLG coated spherical pure Al powder is shown in Fig. 5a. Zeta potential displays surface charge distribution of GO and rGO-LDH during the preparation of Al-GLG powder. GO has negatively charged with a zeta potential of -36.05 mV . The negative zeta potential can be understood as the dissociation of oxygen-containing functional groups ($-\text{OH}$, $-\text{COOH}$) in the graphene oxide (GO) surface. Since LDH has a positive charge, the rGO-LDH has a zeta potential of $+18.03\text{ mV}$, so rGO-LDH and GO attract each other due to electrostatic interaction. Residual oxygen-containing functional groups ($-\text{OH}$, $-\text{COOH}$) on the surface of GO make the rGO-LDH-GO display a zeta potential of -10.77 mV (Fig. 5a) [34,43]. It illustrates that GO can use as a carrier to connect rGO-ZnAl-LDH and aluminum powder. In this process, the GO is reduced by aluminum powder [37]. Fig. S3 shows the FT-IR spectra of Al-GLG powder, the absorption peak at 1641.12 cm^{-1} is the C=C stretching vibration, and the weakness absorption peak at 1062.58 cm^{-1} corresponds to the alkoxy (C—O) stretch vibration, indicating the GLG wrapped on Al powders is reduced graphene oxide

(rGO) [45,50,51]. The absorption band at 3428.81 cm^{-1} results from the stretching vibration of O—H in the metal hydroxyl group [31]. The strong and sharp absorption band centered at 1386.56 cm^{-1} is aroused by the ν_3 mode of NO_3^- in LDH [52]. The band at 557.33 cm^{-1} is mainly attributed to the lattice vibration of M—O [53]. It forms a tightly bound structure material GLG on the surface of aluminum powder. To further demonstrate this tightly bound structure, the charge density differences (CDD) of the rGO-LDH-rGO system (Fig. 5b) are calculated according to

$$\Delta\rho = \rho_{\text{GLG}} - \rho_{\text{rGO-LDH}} - \rho_{\text{rGO}} \quad (5)$$

A strong interaction is excited between the ZnAl-LDH layer and rGO. This indicates strong electrostatic interaction between the ZnAl-LDH layer to rGO. The GLG system also has a good electron transfer according to enhanced DOS (Fig. 5c) and band structure (Fig. 5d), so the GLG system structure is stable. The SEM image of the pure spherical Al powder is in Fig. 5e. The microscopic morphology of the pure spherical Al powder is smooth and neat. Fig. 5f-g shows the SEM image of the 0.2 wt% rGO-coated Al powder microstructure. On the surface of Al powder can be observed a thin, wrinkled film, which is a typical micro-

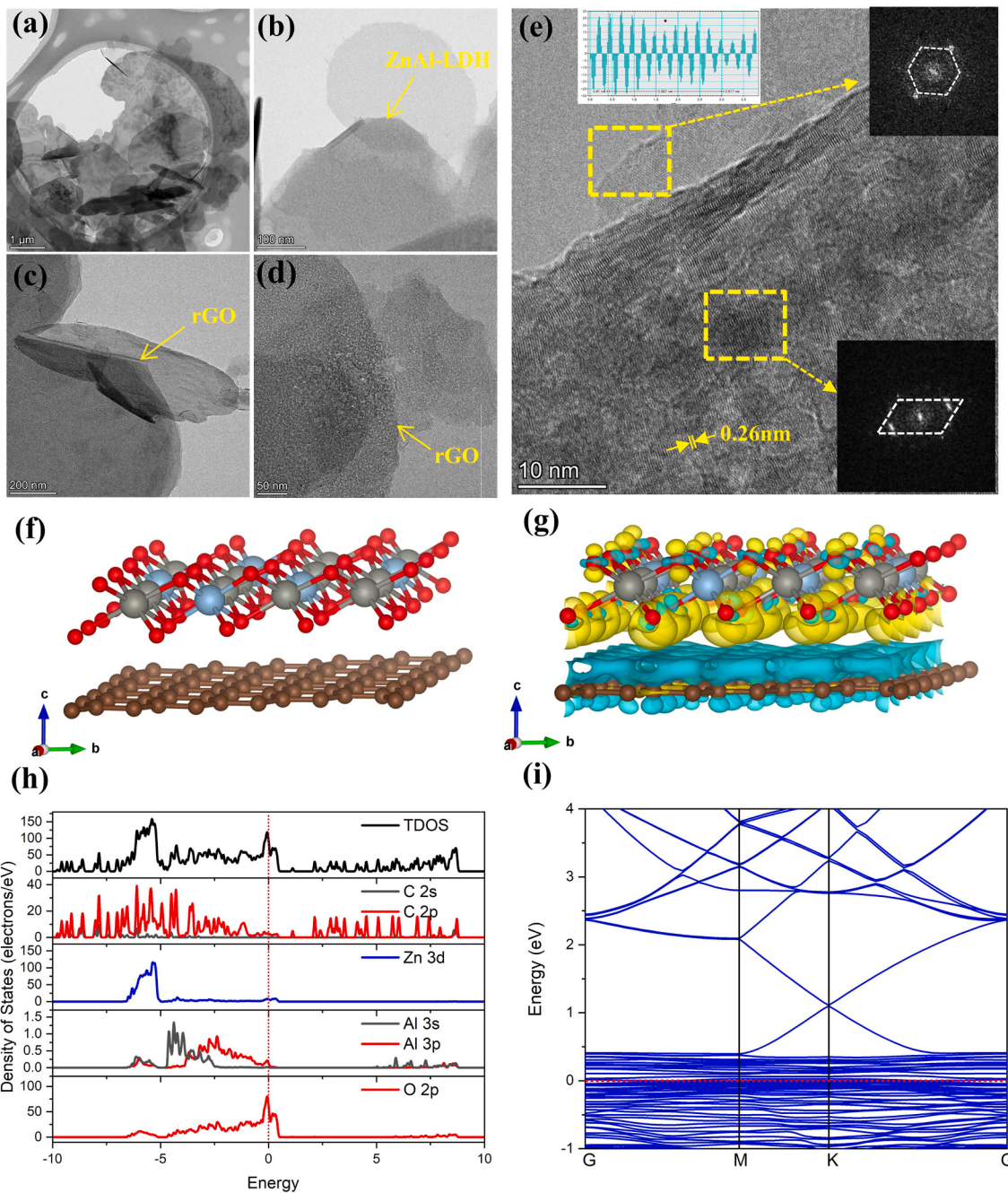


Fig. 4. (a–d) TEM image of rGO-LDH from low to high magnification; (e) HR-TEM image and corresponding Fast Fourier Change (FFT) image. 3D charge density difference (g) and side-view atomic configuration (f) of the rGO-LDH interface system (isosurface value 0.0015 eV/Bohr³). In the 3D plot, the yellow and green regions denote charge accumulation and depletion, respectively. (h) Total and partial calculated density of states (DOS) of rGO-LDH; (i) rGO-LDH band structure. The Fermi level is set to zero.

morphology of graphene [13]. It is revealed that rGO is successfully coated on the Al powder surface as expected. It can be observed that the surface of Al powder is evenly covered by the composite material GLG, which is wrinkled, curled, and scattered nanosheet (Fig. 5h–j). For further verification, EDS element analysis of the surface of Al-GLG powder, it can be found that it corresponds to Zn, Al, N, O, C elements of Fig. 5k. They are typical characteristic elements of Al-GLG powder. The elements' mass ratio of GLG on the surface of Al powder is shown in Fig. S4.

Fig. 6a–c show the cross-sectional SEM image of Al, Al-G, and Al-GLG coating. SEM image of the cross-sectional Al coating (Fig. 6a) exists apparent voids, which appear in the gaps between particles. This

indicates that the Al coating structure is loose and hollow. The cross-sectional SEM image of the Al-G coating (Fig. 6b) shows that the interior of the coating is dense, and there are no apparent pores between the particles. The cross-sectional SEM image of Al-GLG coating (Fig. 6c) shows that the inside is flat and dense, with no obvious defects. Fig. 6d–f show the micromorphology of the cross-sections of Al, Al-G, and Al-GLG coatings after being etched in a 4 vol% NaOH solution for 120 s. The boundary between the particles in the coating was exposed after being etched. Al-G coating (Fig. 6e) can be found that has a wrinkled and curled nanosheet. The corresponding element analysis shows that it is mainly Al and C. It can prove that the wrinkled and curled nanosheet is rGO. The Al-GLG coating (Fig. 6f) also has wrinkled and curled flakes,

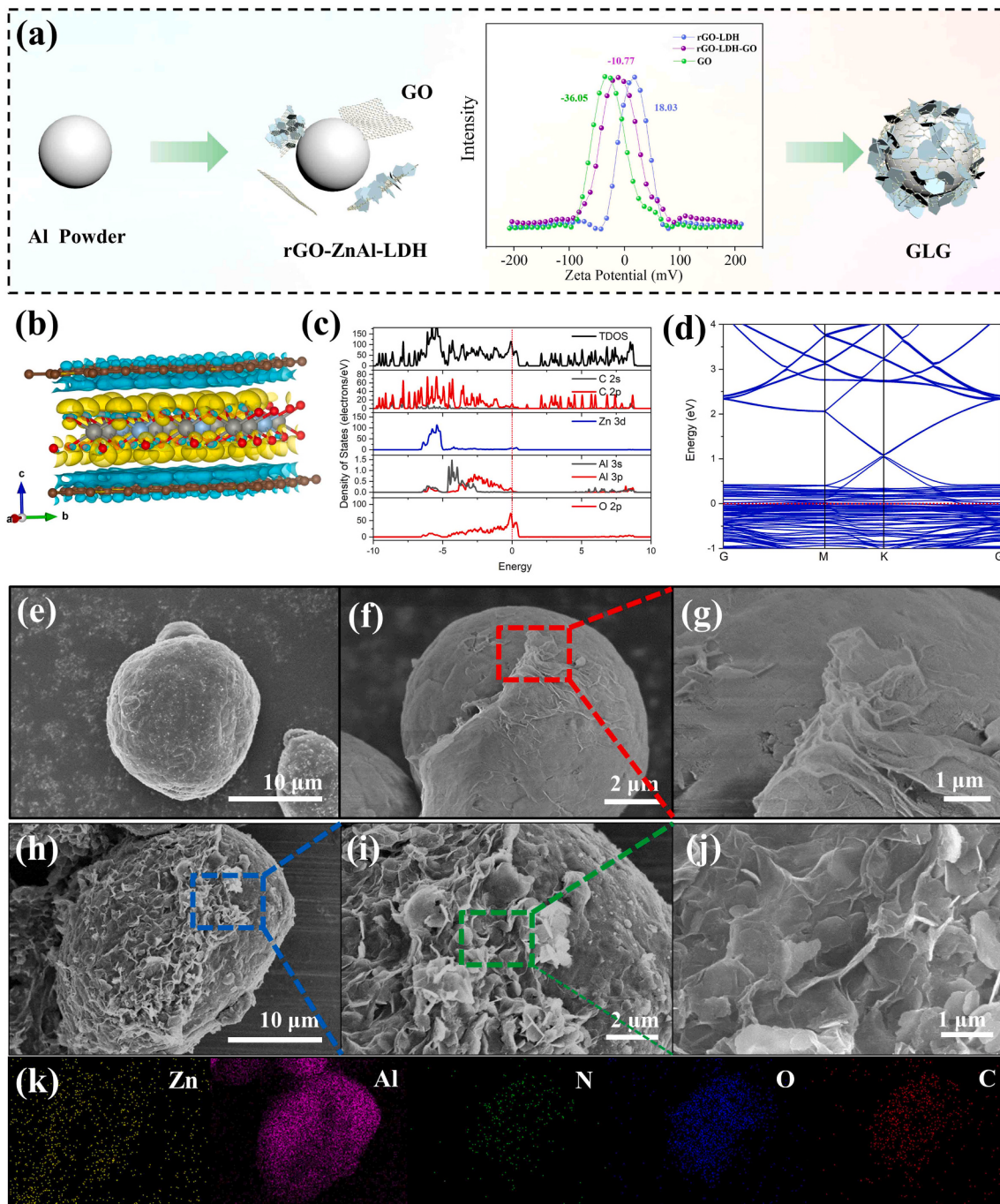


Fig. 5. (a) Schematic diagram of the preparation of Al-GLG powder, inset plots of Zeta potential of GO, rGO-LDH, and rGO-LDH-GO in water; (b) 3D charge density difference of the GLG interface system (isosurface value 0.0015 eV/Bohr³); (c) Total and partial calculated density of states (DOS) of GLG; (d) rGO-LDH band structure. (e) SEM image of spherical pure Al powder; (f, g) SEM image of Al-G powder at different magnification; (h–j) SEM image of Al-GLG powder at different magnification; (k) EDS analysis of Al-GLG powder.

and many small nanosheets are scattered on the cross-section. The corresponding element analysis shows that the microscopic cross-section is mainly Al, Zn, and C. This is a typical characteristic element of rGO-ZnAl-LDH. The XRD patterns of Al, Al-G, and Al-GLG coatings are shown in Fig. 6h. A schematic diagram of the cross-sectional coatings is shown in Fig. 6g. There are pores in the inner gap of the Al coating, Al-G and Al-GLG coatings exist rGO and rGO-ZnAl-LDH in the inner gap, respectively.

The main characteristic diffraction peaks of Al, Al-G and Al-GLG coatings are similar diffraction dominates aluminum peaks. The characteristic diffraction peaks of rGO and ZnAl-LDH in the coating are not

obvious. Additional analysis is needed by Raman spectroscopy, and it is found that “D” and “G” peaks appear in the Al-G coating, which proves that rGO exists in the coating [6,13]. The Al-GLG coating has obvious “M—O—M”, “NO₃”, “D” and “G” peaks, corresponding to “544.25 cm⁻¹”, “1047.44 cm⁻¹”, “1324.76 cm⁻¹”, and “1604.31 cm⁻¹” respectively [28,29] (Fig. 6i). Based on SEM, EDS, XRD, and Raman analysis of the samples, it can verify that introducing GLG inside the aluminum-based composite coating is successful.

Potential dynamic polarization is a known technique that investigates the corrosion resistance of the samples [54]. In the Tafel polarization curve, the magnitude of the self-corrosion potential (E_{corr})

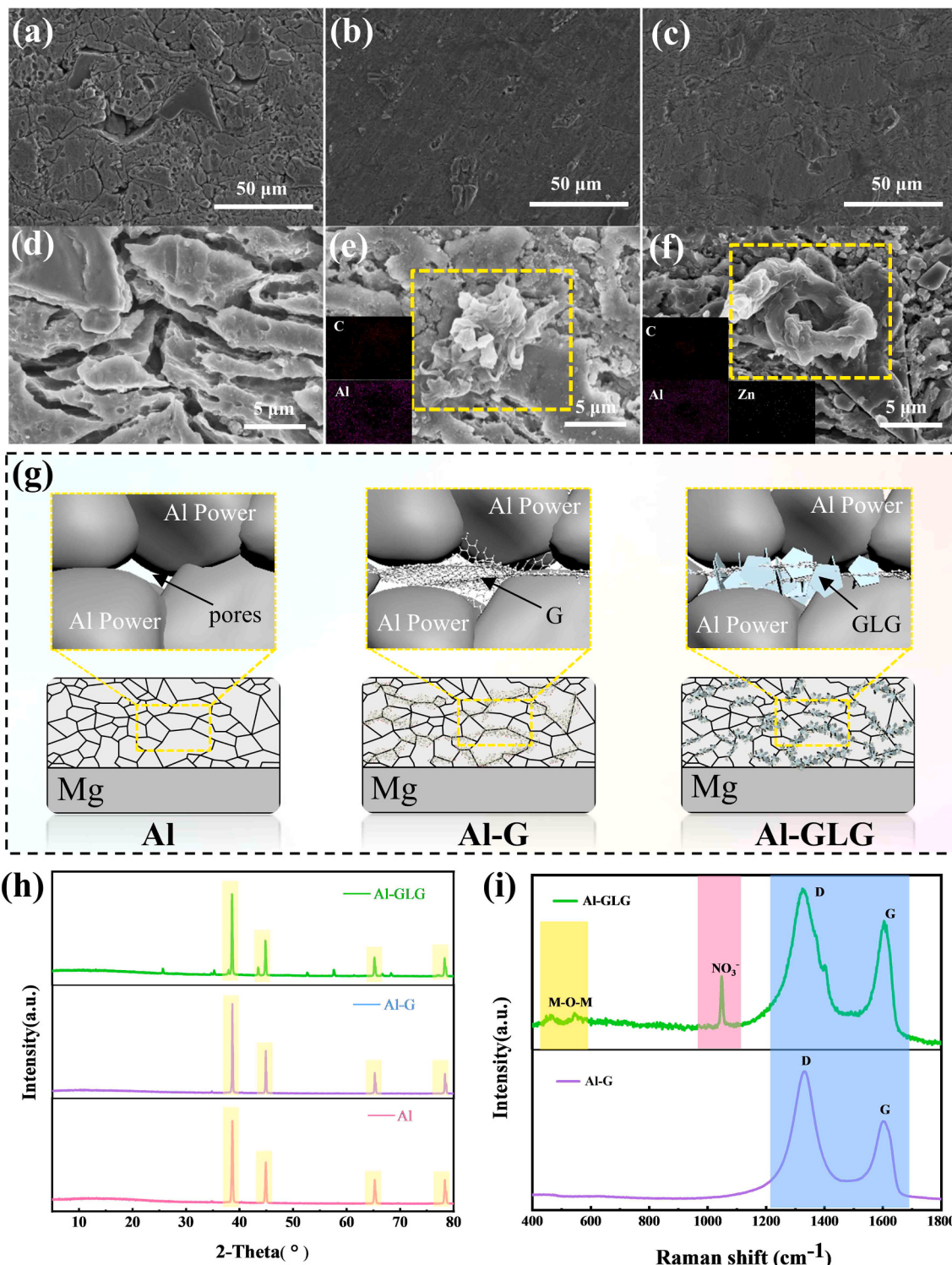


Fig. 6. The cross-sectional SEM image of (a) Al; (b) Al-G and (c) Al-GLG coating; The cross-sectional SEM image of (d) Al; (e) Al-G and (f) Al-GLG coating after etching; (g) Schematic diagram of the cross-sectional of coatings; (h)XRD analysis of Al, Al-G, and Al-GLG coating; (i) Raman spectrum of Al-G and Al-GLG coating.

means the corrosion trend; the strength of the self-corrosion current density (i_{corr}) represents the speed of corrosion [36,55]. Fig. 7a presents the Tafel polarization curve of Mg, Al, Al-G, and Al-GLG samples tested after immersing in 3.5 wt% NaCl solution for 30 min.

It can be found that the E_{corr} of Al-GLG coating is the highest, which is $-0.763 V_{SCE}$ (Fig. 7b). The E_{corr} of Al-G is $-1.13 V_{SCE}$, the E_{corr} of Al is next to Al-G about $-1.283 V_{SCE}$, and the value of The E_{corr} of Mg is the lowest about $-1.52 V_{SCE}$. The E_{corr} of Al-GLG is more positive than that

of Mg, Al, and Al-G coating. And pitting potential of Al-GLG is about $-0.24 V_{SCE}$, which is over 540 mV higher than that of the Al coating.

The self-corrosion current density i_{corr} of Al-GLG is only $0.01287 \mu A \cdot cm^{-2}$ in Fig. 7c. The i_{corr} of Al-GLG is smallest compared with that of Mg, Al, and Al-G coating. The i_{corr} of Al-GLG is three orders of magnitude lower than that of Al coating. Therefore, this result indicates that GLG plays an essential role in Al-GLG coatings to improve the anti-corrosion performance of the aluminum-based coating. By comparing the Tafel

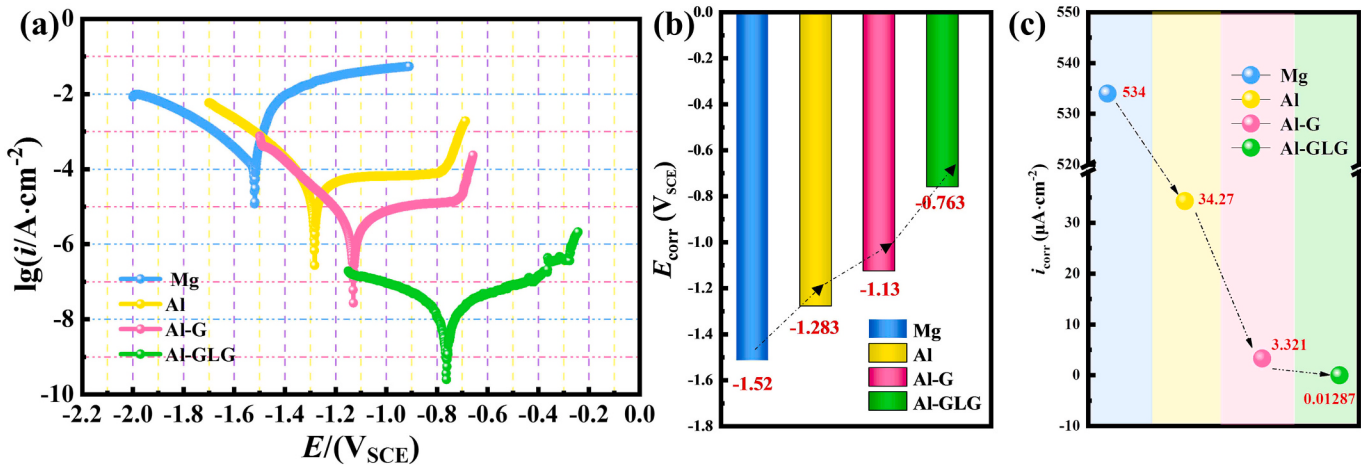


Fig. 7. The Tafel polarization curves (a) and the corresponding self-corrosion potential (b) and self-corrosion current (c) of Mg, Al, Al-G, and Al-GLG coatings.

polarization curve of these samples, it is found that the Al-GLG coating is the most effective in increasing the self-corrosion potential and slowing down the corrosion rate of Mg alloys.

To further evaluate the long-term anti-corrosion of each sample in 3.5 wt% NaCl by EIS. EIS is an important index to assess the performance of coatings to prevent the diffusion/penetration of corrosive media into Mg alloys [11]. Fig. 8a1, b1, c1, and d1 are the Nyquist curves of Al, Al-G, and Al-GLG after immersion for 24 h, 120 h, 240 h, and 360 h. They are composed of a capacitive arc and a diffusion arc, indicating that each coating acts as a barrier to the corrosive medium and involves a mass transfer step during the immersion process. The corrosive medium eroded the defects with a narrow and deep geometry in the coating after immersion for 24 h. In general, the mass transfer behavior of the corrosive medium in the defects leads to the creation of a diffusion arc [11,54]. The semicircle diameter of the capacitive arc radius means the corrosion resistance of the coating [11,55,56]. Fig. 8a3, b3, c3, and d3 show that the Al, Al-G, and Al-GLG only have a time constant during the soaking process, so it can be seen that the coating is always a whole. Therefore, the coating can be regarded as a resistance. With the increase in immersion time, the trend of the capacitive arc of Al, Al-G and Al-GLG in Fig. 8a1, b1, c1, and d1 is that the semicircle diameter increases, and Al-GLG is the most significant. This indicates that the shielding effect of Al-GLG is gradually enhanced during immersion. At the same time, the trend of the Al-GLG diffusion arc in Fig. 8a1, b1, c1, d1 is weakening, indicating that the mass transfer between the Al-GLG coating and the medium is gradually slowing down. This phenomenon is mainly due to two reasons: (1) ZnAl-LDH of the composite material GLG can capture Cl^- during the corrosion process; (2) rGO of the composite material GLG plays a shielding effect in the gap, and a new passivation film is generated during the shielding process. Therefore, under the cooperation of both rGO and ZnAl-LDH, Al-GLG coating owns double protection and great corrosion resistance.

An equivalent circuit (EEC) of $R_{\text{sol}}(Q_1(R_1(R_2L)))$ is used to fit the EIS data of Mg (Fig. 9a). The data analysis is shown in Table 1. R_{sol} stands for solution resistance, R_1 stands for charge transfer resistance, and Q stands for double-layer capacitance. R_2 and L are related to pitting corrosion occurring on the Mg alloy's surface. During the immersion process, the loose corrosion products on the surface cause significant inductance effects [57]. Corrosion products are not resistant to penetration, so magnesium's corrosion resistance remains poor.

To further study the corrosion behavior of Al, Al-G, and Al-GLG coatings. Used equivalent circuit $R_{\text{sol}}(Q_1(R_3(Q_2(R_4Z_w))))$ to fit the EIS data of every sample (Fig. 9b). The data analysis is shown in Table 2, including solution resistance (R_{sol}), coating resistance (R_3), charge transfer resistance (R_4), and Warburg diffusive impedance (Z_w) [54]. And their corresponding capacitances. R_c is the total of R_3 and R_4 are

shown in Table 3. In theory, the larger the value of R_c , the better the anti-corrosion and lower charge transfer. As the immersion time increases, the values of R_c of Al continue to decrease. This is due to the corrosive medium infiltrating into the coating. The values of R_c of Al-G increase after soaking 120 h, which illustrates that the passivation film on the surface of Al-G is forming. As the immersion time increases, the values of R_3 decrease. It is caused by Cl^- penetrating corrosion of the interior of the coating. The values of R_c of Al-GLG reach a maximum of $8.096 \times 10^4 \Omega \cdot \text{cm}^2$ after soaking for 120 h. At this time, a uniform and complete passivation film is formed on the surface of Al-GLG, which hinders the transfer of charge. On the one hand, GLG in the Al coating blocks the corrosive medium during the infiltration process, generating corrosive production to fill the coating gap, and enhancing the coating resistance R_3 . On the other hand, the surface passivation film continued to form due to ZnAl-LDH capturing Cl^- at the early stage of corrosion. The surface passivation film mainly consisted of Al_2O_3 and has a low conductivity, so the value of the charge transfer resistance R_4 increased to $6.926 \times 10^4 \Omega \cdot \text{cm}^2$. The corrosive medium's mass transfer behavior occurs at the coating's defects. Aluminum-based coatings are mainly characterized by pitting corrosion. The more active the pitting corrosion, the more loose corrosion products are produced in the defect, and the corresponding Z_w is also larger [11,58]. Al-GLG due to the presence of ZnAl-LDH at coating defects. ZnAl-LDH can trap Cl^- and slow down the generation of loose corrosion products, so the Z_w value of Al-GLG coating is less than that of Al-G and Al [54]. The R_c value of Al-GLG is an order of magnitude higher than that of Al-G and Al and remains high throughout the immersion process. Therefore, it indicates the Al-GLG coating has an excellent long-term protection effect.

The $|Z|_{0.01\text{Hz}}$ plays a vital role in estimating the long-term protective effect of the coating (Fig. 10a) [55,56]. The $|Z|_{0.01\text{Hz}}$ of Al-GLG remains at $3.66 \times 10^4 \Omega \cdot \text{cm}^2$ after being soaked for 360 h. The $|Z|_{0.01\text{Hz}}$ of Al-GLG is less variable from 24 h to 360 h, as shown in Fig. 8a2, b2, c2, and d2. While after being soaked for 360 h, the $|Z|_{0.01\text{Hz}}$ of Al-G decreases to $1.11 \times 10^4 \Omega \cdot \text{cm}^2$, the $|Z|_{0.01\text{Hz}}$ of Al is close to Al-G at about $7.39 \times 10^3 \Omega \cdot \text{cm}^2$. The $|Z|_{0.01\text{Hz}}$ of Mg alloy remains stable at a low level of about $3.99 \times 10^2 \Omega \cdot \text{cm}^2$. The $|Z|_{0.01\text{Hz}}$ of Mg, Al, and Al-G are all smaller than that of Al-GLG ($3.66 \times 10^4 \Omega \cdot \text{cm}^2$). These results illustrate that Al-GLG has long-term effective corrosion resistance.

In theory, the higher R_c reflects the better anti-corrosion and lower charge transfer. After immersion for 360 h, the Al-GLG shows the highest R_c value of $7.21 \times 10^4 \Omega \cdot \text{cm}^2$ (Fig. 10b), it is larger than the R_c value of Al-G ($8.60 \times 10^3 \Omega \cdot \text{cm}^2$) and Al ($3.05 \times 10^3 \Omega \cdot \text{cm}^2$). Implying that Al-GLG has the highest anti-corrosion and lowest charge transfer in saline solution. And the synergy effect of rGO and ZnAl-LDH in Al-GLG coating can restrain the corrosive medium and reduce the corrosion rate from attacking the Mg alloy.

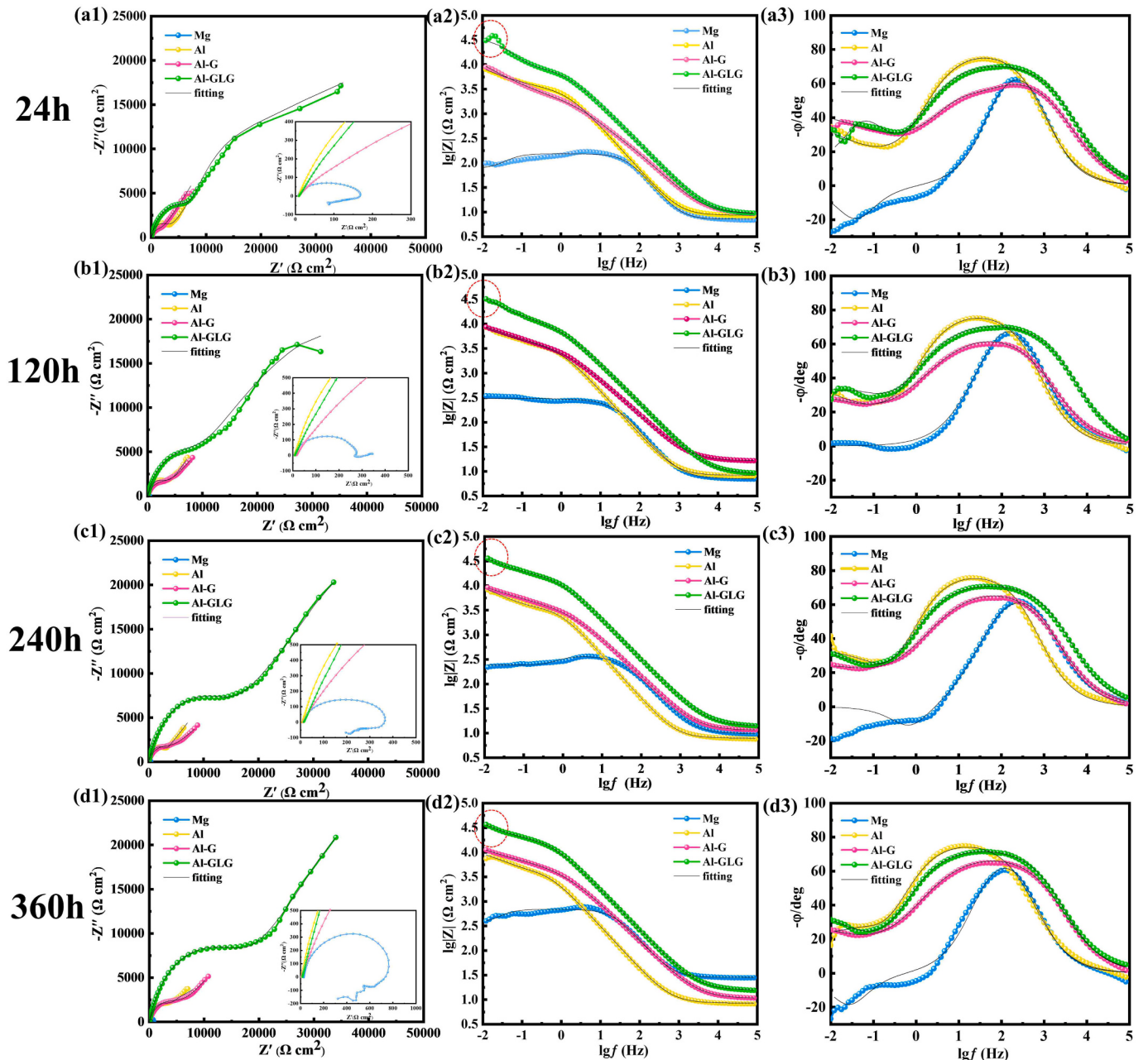


Fig. 8. The EIS of Mg, Al, Al-G, Al-GLG in 3.5 wt% NaCl solution for 24 h, 120 h, 240 h, 360 h: (a1, b1, c1, d1) correspond to the Nyquist diagram of Mg, Al, Al-G, Al-GLG; (a2, a3, b2, b3, c2, c3, d2, d3) are corresponding to Bode plot of Mg, Al, Al-G, Al-GLG.

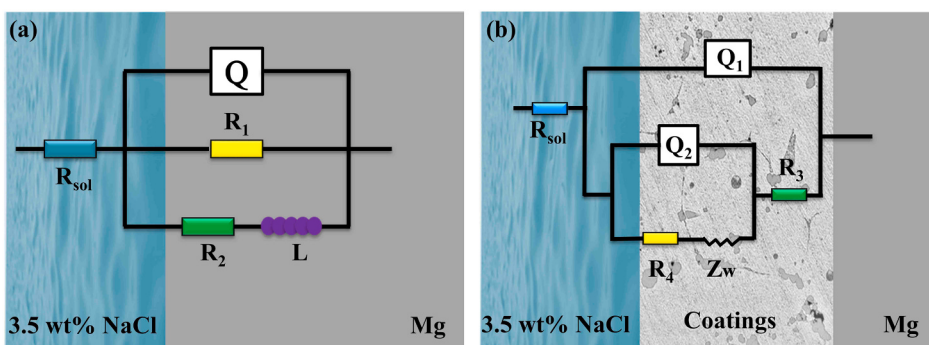


Fig. 9. (a) Equivalent circuit of Mg; (b) Equivalent circuit of Al, Al-G, Al-GLG.

Table 1

EIS parameters for Mg.

Samples	Hour	$R_{\text{sol}} (\Omega \cdot \text{cm}^2)$	$Q \cdot Yo (\Omega^{-1} \cdot \text{cm}^2 \cdot \text{s}^{-1})$	Q-n	$R_1 (\Omega \cdot \text{cm}^2)$	L	$R_2 (\Omega \cdot \text{cm}^2)$	x^2
Mg	24 h	7.163	2.976×10^{-5}	0.9568	146.6	712.3	135	1.205×10^{-3}
	120 h	7.047	5.741×10^{-5}	0.8791	528.8	0.5123	313.7	4.127×10^{-3}
	240 h	9.732	2.667×10^{-5}	0.8711	364.9	178.6	638.4	1.225×10^{-3}
	360 h	28.49	1.516×10^{-5}	0.9339	661.4	5652	655.6	9.715×10^{-4}

Table 2

EIS parameters for Al, Al-G and Al-GLG coatings.

Hour	Samples	$R_{\text{sol}} (\Omega \cdot \text{cm}^2)$	$Q \cdot Yo (\Omega^{-1} \cdot \text{cm}^2 \cdot \text{s}^{-1})$	Q-n	$R_3 (\Omega \cdot \text{cm}^2)$	$Q \cdot Yo (\Omega^{-1} \cdot \text{cm}^2 \cdot \text{s}^{-1})$	Q-n	$R_4 (\Omega \cdot \text{cm}^2)$	$Z_w (\Omega^{-1} \cdot \text{cm}^2 \cdot \text{s}^{-1/2})$	x^2
24 h	Al	8.599	4.234×10^{-5}	0.8973	252.3	1.576×10^{-5}	0.7937	3.140×10^3	6.530×10^{-4}	9.905×10^{-4}
	Al-G	9.076	4.038×10^{-5}	0.7782	787.8	2.229×10^{-5}	0.8638	3.221×10^3	4.362×10^{-4}	3.899×10^{-4}
	Al-GLG	9.250	2.133×10^{-5}	0.8156	9872	1.737×10^{-4}	0.9488	3.236×10^4	3.348×10^{-4}	4.811×10^{-3}
	Al	8.316	5.594×10^{-5}	0.8950	115.1	1.246×10^{-5}	0.7961	3.497×10^3	6.367×10^{-4}	8.563×10^{-4}
	Al-G	16.21	4.876×10^{-5}	0.7722	728	8.522×10^{-5}	0.2694	5.083×10^3	3.920×10^{-4}	2.516×10^{-4}
	Al-GLG	9.010	2.209×10^{-5}	0.8133	11,700	1.633×10^{-4}	0.6533	6.926×10^4	3.281×10^{-4}	5.462×10^{-4}
	Al	7.895	6.414×10^{-5}	0.8921	398.4	8.848×10^{-5}	0.9874	2.229×10^3	6.516×10^{-4}	1.015×10^{-3}
	Al-G	11.37	4.09×10^{-5}	0.7965	180.7	9.008×10^{-5}	0.1752	7.245×10^3	2.717×10^{-4}	1.861×10^{-4}
	Al-GLG	14.03	1.608×10^{-5}	0.8193	19,060	1.874×10^{-4}	0.9844	5.579×10^4	1.519×10^{-4}	3.221×10^{-4}
360 h	Al	8.504	8.608×10^{-5}	0.8742	50.24	9.484×10^{-5}	0.9775	3.004×10^3	6.040×10^{-4}	1.856×10^{-3}
	Al-G	10.50	3.891×10^{-5}	0.7932	77.73	4.910×10^{-5}	0.1993	8.528×10^3	3.489×10^{-4}	1.911×10^{-4}
	Al-GLG	15.59	1.854×10^{-5}	0.8270	21,340	2.118×10^{-4}	0.9973	5.084×10^4	1.410×10^{-4}	3.630×10^{-4}

Table 3

Resistance parameters for Al, Al-G and Al-GLG coatings.

Hour	Samples	$R_3 (\Omega \cdot \text{cm}^2)$	$R_4 (\Omega \cdot \text{cm}^2)$	$R_c = R_3 + R_4 (\Omega \cdot \text{cm}^2)$
24 h	Al	252.3	3.140×10^3	3392.3
	Al-G	787.8	3.221×10^3	4008.8
	Al-GLG	9872	3.236×10^4	42,232
120 h	Al	115.1	3.497×10^3	3612.1
	Al-G	728	5.083×10^3	5811
	Al-GLG	11,700	6.926×10^4	80,960
240 h	Al	398.4	2.229×10^3	2627.4
	Al-G	180.7	7.245×10^3	7425.7
	Al-GLG	19,060	5.579×10^4	74,850
360 h	Al	50.24	3.004×10^3	3054.24
	Al-G	77.73	8.528×10^3	8605.73
	Al-GLG	21,340	5.084×10^4	72,180

The largest value of low-frequency impedance modulus $|Z|_{0.01\text{Hz}}$ and R_c indicate the best long-term effective corrosion resistance and lower charge transfer. The essence of corrosion reaction is charge transfer. The lower charge transfer of Al-GLG prevents corrosive media from

damaging the Mg alloy. As a result, Al-GLG has a high resistance to corrosion media. A schematic diagram of the charge transfer of samples is shown in Fig. 10c. GLG in the aluminum-based composite coating plays a vital role against corrosion medium.

After immersion in 3.5 wt% NaCl solution for 24 h, 120 h, 240 h, and 360 h, the macroscopic corrosion morphology of Mg, Al, Al-G, and Al-GLG are observed by an optical microscope. It can be seen that Mg is severely corroded in Fig. 11a1–a4. With the exceeding immersion time, many pits with white corrosion products are formed on the surface of Mg. Multiple pitting pits with white products are included on the surface of the Al coating. The pitting corrosion is severe during the immersion process, which can be clearly observed in Fig. 11b1–b4. The surface of the Al-G coating keeps intact during the initial immersion (Fig. 11c2). After immersion for 240 h (Fig. 11c3), pitting corrosion appears on the surface of the Al-G coating. After immersion for 360 h (Fig. 11c4). White corrosion products appear around the pitting pores. However, on the surface of Al-GLG coating, a few pitting corrosion begin to appear, and the surface morphology of the coating is complete after immersion for 360 h (Fig. 11d1–d4). It has been proved that the Al-GLG coating has the best protection effect.

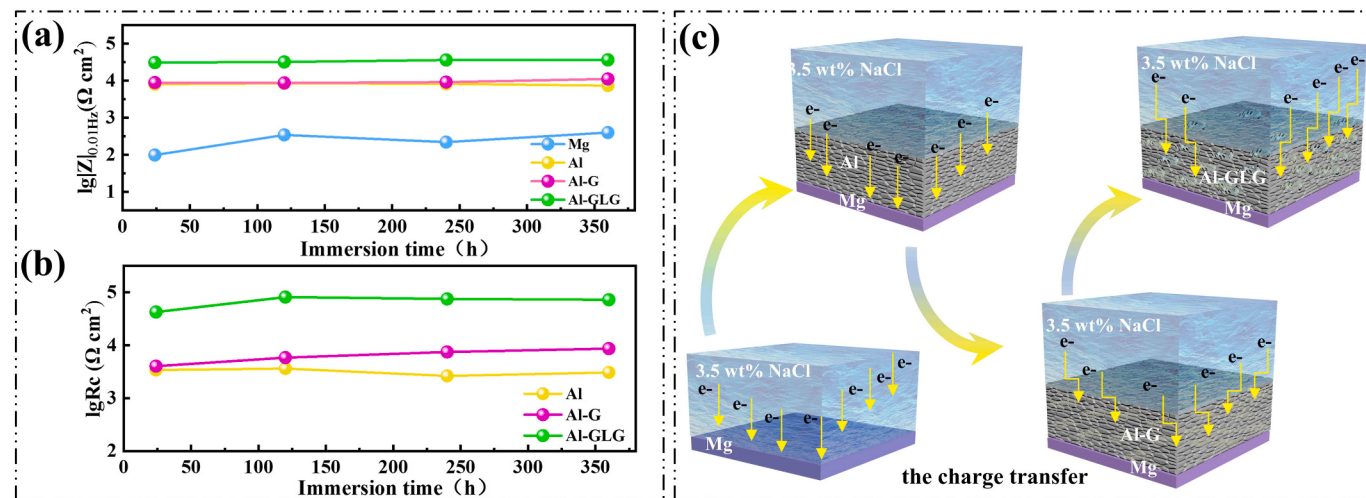


Fig. 10. (a) The correlation between immersion time and $\lg|Z|_{0.01\text{Hz}}$; (b) $\lg R_c$ of samples at 24 h, 120 h, 240 h, and 360 h of immersion; (c) Schematic diagram of the charge transfer of samples.

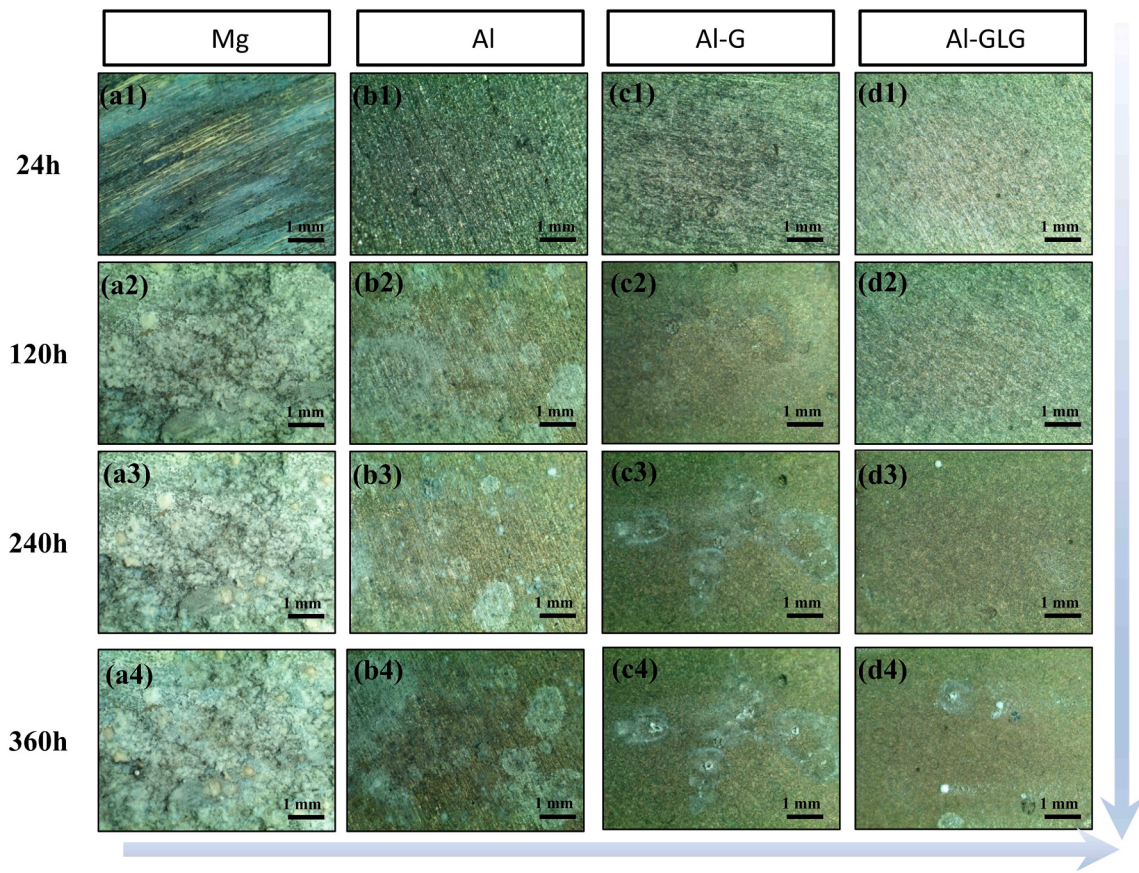


Fig. 11. Optical micrographs of corrosion morphology for (a1–a4) Mg, (b1–b4) Al, (c1–c4) Al-G, (d1–d4) Al-GLG after immersion in 3.5 wt% NaCl solution after 24 h, 120 h, 240 h, and 360 h.

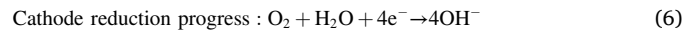
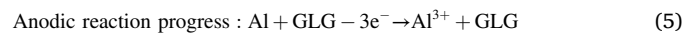
To study the details of the corrosive medium penetrating through the coating after immersion for 360 h, it characterized the morphology of the surface and cross-section of the coating. The surface of Mg is severely eroded. The loose corrosion products appear in the corrosion pits (Fig. 12a); loose corrosion products appear on the surface of the Al coating, and the corrosion pits are dense (Fig. 12b). The corrosion pits of Al-G can be seen in the wrinkled G sheets. The corrosive medium penetrates the graphene and erases the aluminum particle, which appears to have cracks (Fig. 12c). In contrast, a few pits appear on the Al-GLG coating surface, and the pitting area is small (Fig. 12d).

SEM of the cross-sectional morphology of Mg, Al, Al-G, and Al-GLG coatings. The corrosive medium has severely corroded Mg, and a large area of depression appears at the cross-sectional, as shown in Fig. 12e. The cross-sectional of the Al coating can be observed that the corrosive medium has penetrated along the pitting pit longitudinally. The corrosive medium has eroded to the Mg substrate. The corrosion products separate the coating and the substrate (Fig. 12f). It can be seen from the cross-sectional of the Al-G coating that many corrosives concentrate on the surface, and there is no corrosion along the vertical direction of the coating (Fig. 12g). The cross-section of the Al-GLG coating keeps good integrity, and the protective effect is pronounced (Fig. 12h).

Comparison of the corrosion state of the samples (Fig. 12i), the order of the size of the corrosion area is Mg > Al > Al-G > Al-GLG, and Al-GLG has the smallest corrosion area. From the cross-sectional morphology, the Mg has corrosion pits, and the Al coating has micro-cracks. However, only a small amount of corrosion products exist on the surface of the Al-GLG coating after immersion for 360 h.

To further study the phase of the corrosion products, it analyzes the phase of the samples' XRD after immersion for 360 h, and it finds that the white corrosion products on the surface of Al, Al-G, and Al-GLG coatings are mainly Al_2O_3 , AlOOH , $\text{Al}(\text{OH})_3$, and AlCl_3 . $\text{Mg}(\text{OH})_2$ is formed on the

surface of Mg (Fig. 12j). The XRD results with ICDD reference codes of the representative sample of Mg and Al-GLG are shown in Fig. S5. The GLG can't dissolve as the cathode when the immersion process of the Al-GLG coating in 3.5 wt% NaCl. According to the series of relevant theories and XRD analyses, the main corrosion reaction solution was as follows [63,64]:



With the continuous immersion of the corrosive medium, the OH^- , Cl^- and Al^{3+} continue to undergo corrosion reactions as follows:



In addition, in terms of metal-based anti-corrosion coatings on Mg alloy, the comparison of self-corrosion potential, self-corrosion current, and full immersion time among designed Al-GLG coating and similar metal-based coatings using rGO or LDH are shown in Fig. 12k. The corrosion resistance of the Al-GLG coatings prepared using this approach outweighed that of the LDH coatings formed on the surface of metal alloys using the in situ synthesis method. Designed Al-GLG coating has obvious advantages in self-corrosion potential, self-corrosion current, and full immersion corrosion life.

The finite element analysis of the electrolyte potential on the surface of magnesium alloy and aluminum-based coating (Fig. 13a) can analyze

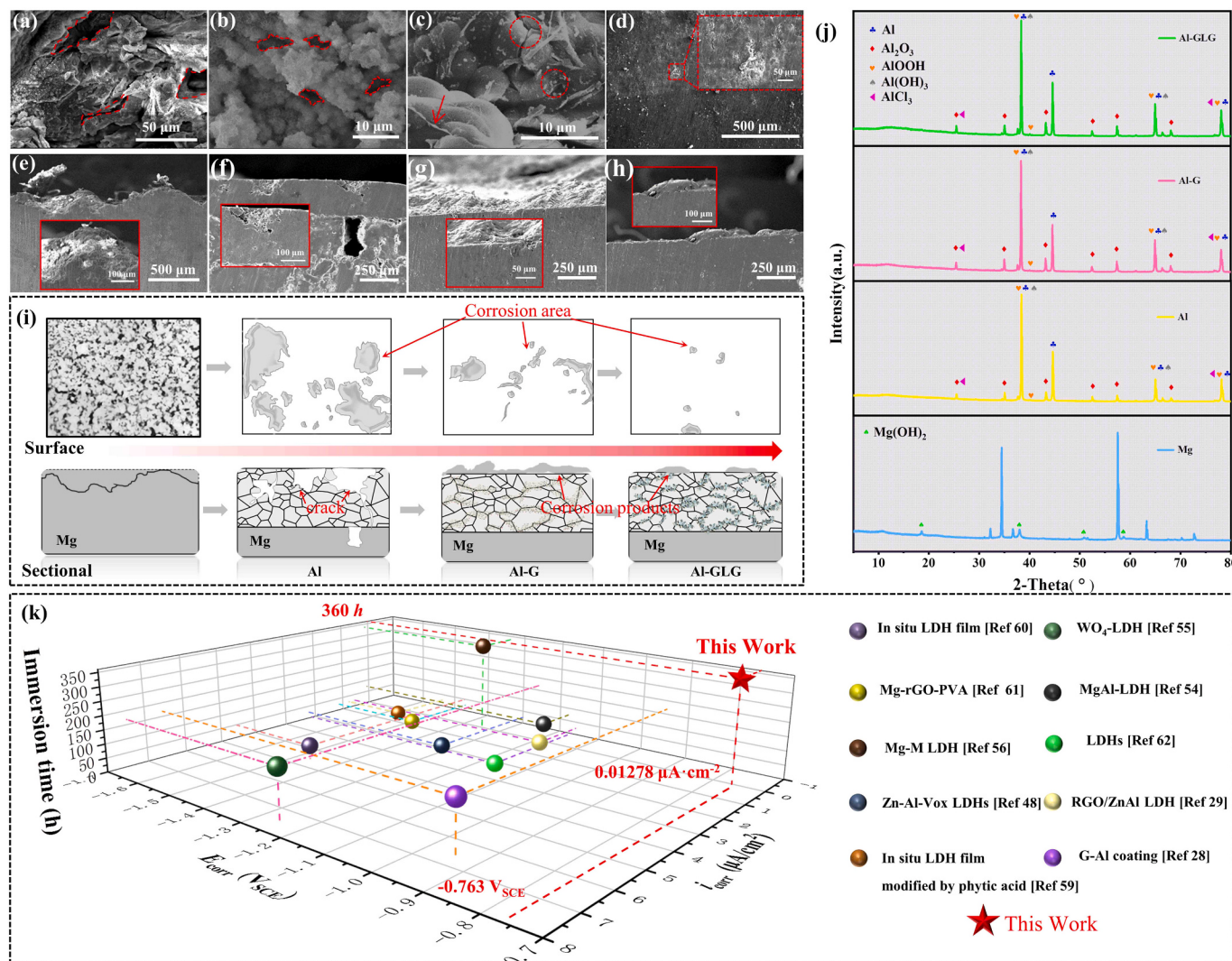


Fig. 12. SEM images of the corrosion morphology of (a) Mg, (b) Al, (c) Al-G, (d) Al-GLG; SEM images of the corresponding corrosion sectional of (e) Mg, (f) Al, (g) Al-G, (h) Al-GLG; (i) Schematic diagram of the corrosion condition of the surface and sectional; (j) XRD analysis of Mg, Al, Al-G, Al-GLG in 3.5 wt% NaCl after being soaked for 360 h; (k) anti-corrosion ability comparison of the metal-based coating using rGO, LDH on Mg alloy [28,29,48,54–56,59–62].

the corrosion distribution on the surface of magnesium alloy and aluminum-based coating. The greater the electrolyte potential, the more serious the corrosion is by 3.5 wt% NaCl. From the finite element analysis, with the increase of time, the surface of magnesium alloy has severe corrosion depression. The aluminum-based coating without GLG will have to pit corrosion, and the pitting hole becomes more profound and broader. An excellent protection system needs to improve both situations. Al-GLG has the best corrosion resistance. The anti-corrosion mechanisms are found in this work in the following two aspects (Fig. 13b):

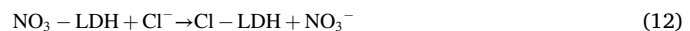
(1) Corrosion resistance mechanism of the ZnAl-LDH

During immersion corrosion, according to the formula generated from corrosion products (7)–(9), it can simplify to the following formula:



In the whole corrosion process, the final corrosion product of aluminum-based coating is Al_2O_3 and AlCl_3 . In the immersion process, the GLG can capture Cl^- by the ZnAl-LDH, which has a corrosion

inhibition effect (Fig. 13b). The Raman results of Al-GLG coating's pitting area in 3.5 wt% NaCl after being soaked for 24 h, 120 h, 240 h, and 360 h are shown in Fig. S6. It can be observed that the characteristic peaks of NO_3^- gradually weaken; the process is as follows [28,65]:



Therefore, inhibiting the generation of AlCl_3 can promote the generation of Al_2O_3 , which is the main component of the passive film. XPS analyzes the chemical state around the pitting area of the Al-GLG coating after immersion in 3.5 wt% NaCl solution for 360 h, the peaks of Al_2O_3 are the main corrosion production (Fig. S7). So the charge transfer resistance (R_4) on the surface of Al-GLG coating remains at a high level.

(2) Corrosion resistance mechanism of the rGO

The rGO dispersed inside the aluminum-based coating has a physical barrier effect on corrosive media. The aluminum-based coating has serious pitting corrosion phenomena, resulting in micropores and defects. These micropores lead to the corrosion medium penetrating the coating and eroding the substrate. The rGO with a two-dimensional layered structure has a physical shielding effect, which hinders the

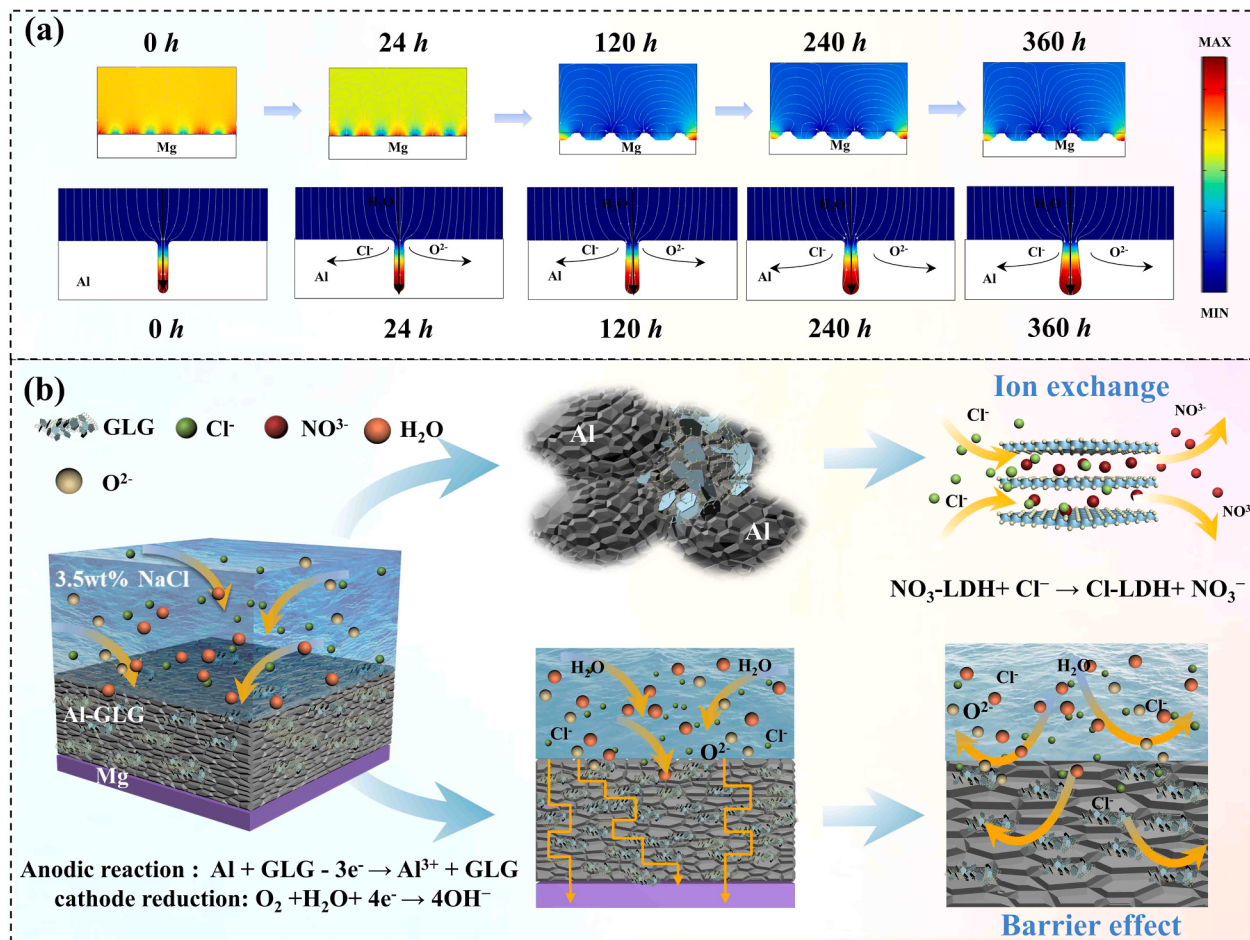


Fig. 13. (a) Finite element analysis (FEA) of the corrosion distributions of Mg alloy and aluminum-based coating; (b) Schematic diagram of the anti-corrosion mechanism of Al-GLG coating.

penetration of corrosive media [6].

(3) Corrosion tendency

The main cause of pitting corrosion in aluminum-based coatings is the action of occluded corrosion cell (OCC) [66–68]. The Al-G coating only has a shielding effect during immersion (Fig. 14a). Severe pitting corrosion occurs on aluminum coating, and the corrosive medium erodes through the coating to the substrate (Fig. 14a). The reason is that the Cl⁻ inside the pitting hole constantly erodes to produce the corrosion product AlCl₃, which promotes the continuous dissolution of aluminum at the bottom of the pitting hole. A large amount of Al³⁺ reacts with OH⁻ at the pitting orifice to form Al(OH)₃, which can block the pitting hole. It prevents OH⁻ from entering the pitting hole and hinders passive film formation in the pitting hole.

However, when the corrosive medium erodes the Al-GLG coating (Fig. 14c), the rGO hinders the propagation of corrosive media deep into the coating, and ZnAl-LDH captures Cl⁻ and replaces the nitrate ions [28], which has slowed down the dissolution of aluminum at the bottom of the pitting hole. With the synergy of the rGO and ZnAl-LDH, fewer corrosion products are produced and reduce the occlusion of the etching hole. This facilitates the exchange of OH⁻ inside and outside the pitting corrosion pores. According to the formula (10), it promotes the formation of Al₂O₃ passivation film inside the pitting corrosion pores. It successfully hinders the expansion of pit holes. It is manifested as an increase in the coating resistance (R_3) of the Al-GLG coating. The schematic diagram of the mechanism is shown in Fig. 14. The Al-GLG coating effectively slows down the tendency of longitudinal corrosion.

4. Conclusion

Aluminum powder modified by GLG was successfully deposited on the surface of the magnesium alloy by low-pressure cold spraying to form a protective Al-GLG coating, and its anti-corrosion properties were investigated in detail. The advantages are as follows:

1. Using in situ growth and electrostatic attraction method, it was formed a stable rGO-LDH-rGO (GLG) on the surface of aluminum powder. And then, it effectively solved the issues of ZnAl-LDH and rGO: the difficulty of dispersion, poor fluidity, and bad compatibility with metal powders.
2. The physical shielding effect of rGO and the corrosion inhibition of ZnAl-LDH synergistically weaken the occluded corrosion cell (OCC) action. It effectively reduced the pitting damage and prolonged the corrosion resistance life of the Al-GLG coating.
3. Given rGO and ZnAl-LDH synergy, it was believed that the Al-GLG coating slowed down the tendency of longitudinal corrosion and increased the pitting resistance of the Al-GLG coating.
4. rGO and ZnAl-LDH reinforced aluminum-based coating as a nanomaterial-metal protection system exhibited excellent anti-corrosion properties. It provided new horizons in the field of metal surface protection.

CRediT authorship contribution statement

Liuyan Zhang and Gengzhe Shen designed this work and analyzed the data; *Gengzhe Shen, Huishu Wu, Zhiwei Gu and Yuwen Liu* fabricated,

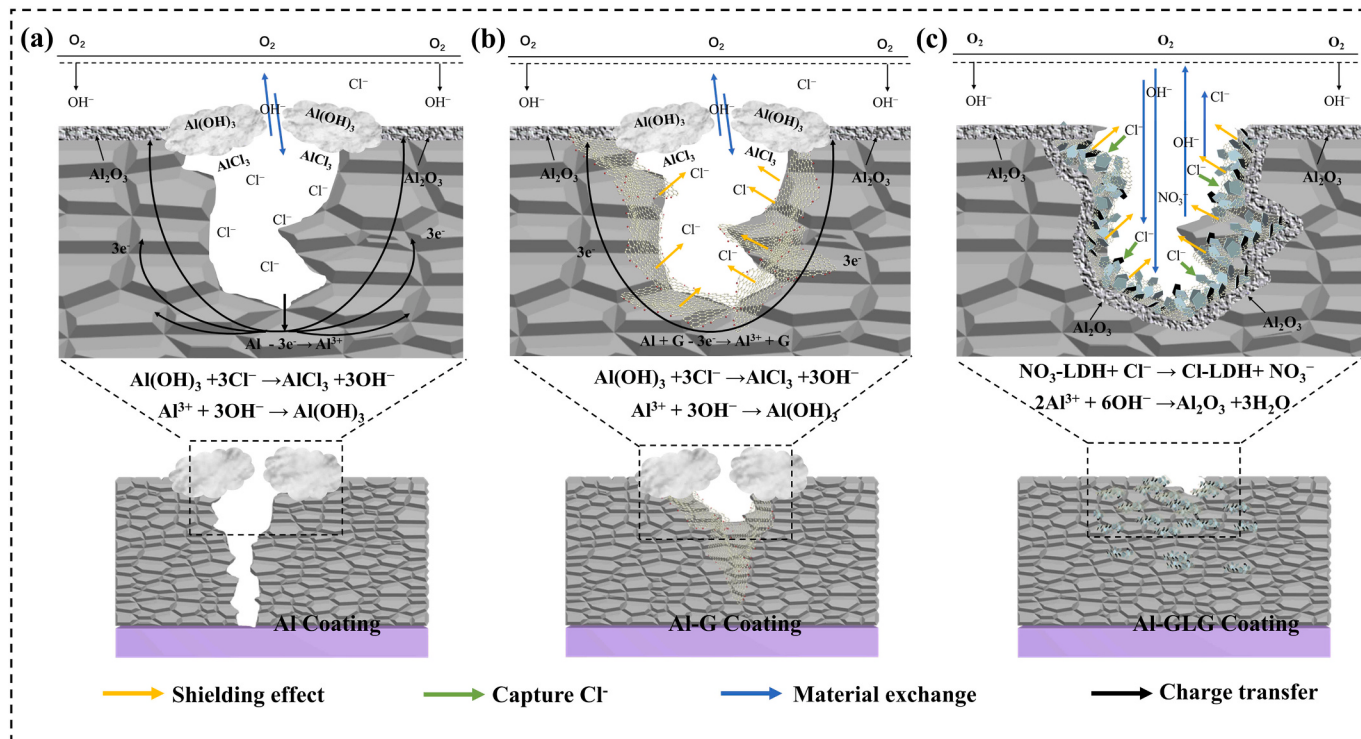


Fig. 14. Schematic diagram of the mechanism of pitting corrosion of Al (a), Al-G (b), and Al-GLG (c) coatings in 3.5 wt% NaCl.

characterized the sample; *Gengzhe Shen, Liuyan Zhang, Shixuan Wang, Qiongbin Zheng and Guibin Tan* discussed the results; *Gengzhe Shen and Xiaohua Jie* involved in the analysis of characterization; *Gengzhe Shen* wrote the manuscript; *Liuyan Zhang* revised the manuscript. All authors read and approved the final manuscript.

Declaration of competing interest

The authors declare that they have no known competing financial interests or personal relationships that could have appeared to influence the work reported in this paper.

Data availability

The raw/processed data required to reproduce these findings cannot be shared at this time as the data also forms part of an ongoing study.

Acknowledgments

This work was supported by the National Natural Science Foundation of China (No. 52105176, No. 51709049), the National Key Research and Development Program of China (2021YFB3400601), the Program for Guangdong Introducing Innovative and Entrepreneurial Teams (2019BT02Z393), the Youth Innovative Talents Project of Guangdong Province (2021KQNCX098), Dongguan Social Science and Technology Development Key Project (No. 2021A1515110154). Besides, the authors gratefully acknowledge Hangzhou Yanqu Information Technology Co., Ltd. for providing First-principles calculations analysis services.

Appendix A. Supplementary data

Supplementary data to this article can be found online at <https://doi.org/10.1016/j.surfcoat.2022.128878>.

References

- [1] I.B. Singh, M. Singh, S. Das, A comparative corrosion behavior of Mg, AZ31 and AZ91 alloys in 3.5% NaCl solution, *J. Magnes. Alloys* 3 (2) (2015) 142–148.
- [2] M. Esmaily, J.E. Svensson, S. Fajardo, N. Birbilis, G.S. Frankel, S. Virtanen, R. Arrabal, S. Thomas, L.G. Johansson, Fundamentals and advances in magnesium alloy corrosion, *Prog. Mater. Sci.* 89 (2017) 92–193.
- [3] S. Mohamed, S. Friedrich, B. Friedrich, Refining principles and technical methodologies to produce ultra-pure magnesium for high-tech applications, *Metals* 9 (2019) 1.
- [4] L. Han, Z. Zhang, J. Dai, X. Li, J. Bai, Z. Huang, C. Guo, F. Xue, C. Chu, The influence of alternating cyclic dynamic loads with different low frequencies on the bio-corrosion behaviors of AZ31B magnesium alloy *in vitro*, *Bioact. Mater.* 7 (2022) 263–274.
- [5] Q. Wang, Q. Sun, M.-X. Zhang, W.-J. Niu, C.-B. Tang, K.-S. Wang, X. Rui, L. Zhai, L. Wang, The influence of cold and detonation thermal spraying processes on the microstructure and properties of Al-based composite coatings on Mg alloy, *Surf. Coat. Technol.* 352 (2018) 627–633.
- [6] X. Wang, L. Zhang, X. Zhou, W. Wu, X. Jie, Corrosion behavior of Al2O3-reinforced graphene encapsulated Al composite coating fabricated by low pressure cold spraying, *Surf. Coat. Technol.* 386 (2020).
- [7] N. Li, L. Zhang, M. Xu, T. Xia, X. Ruan, S. Song, H. Ma, Preparation and mechanical property of electrodeposited Al-graphene composite coating, *Mater. Des.* 111 (2016) 522–527.
- [8] H.R. Bakhshehi-Rad, E. Hamzah, A.F. Ismail, M. Aziz, E. Karamian, N. Iqbal, Bioactivity, in-vitro corrosion behavior, and antibacterial activity of silver-zeolites doped hydroxyapatite coating on magnesium alloy, *Trans. Nonferrous Met. Soc. China* 28 (8) (2018) 1553–1562.
- [9] H. Assadi, H. Kreye, F. Gärtner, T. Klassen, Cold spraying – a materials perspective, *Acta Mater.* 116 (2016) 382–407.
- [10] A. Moridi, S.M. Hassani-Gangaraj, M. Guagliano, M. Dao, Cold spray coating: review of material systems and future perspectives, *Surf. Eng.* 30 (6) (2014) 369–395.
- [11] Y. Tao, T. Xiong, C. Sun, L. Kong, X. Cui, T. Li, G.-L. Song, Microstructure and corrosion performance of a cold sprayed aluminium coating on AZ91D magnesium alloy, *Corros. Sci.* 52 (10) (2010) 3191–3197.
- [12] K. Spencer, D.M. Fabijanic, M.X. Zhang, The use of Al-Al2O3 cold spray coatings to improve the surface properties of magnesium alloys, *Surf. Coat. Technol.* 204 (3) (2009) 336–344.
- [13] H. Wu, Y. Zhang, S. Long, L. Zhang, X. Jie, Tribological behavior of graphene anchored Mg-Al layered double hydroxide film on Mg alloy pre-sprayed Al coating, *Appl. Surf. Sci.* 530 (2020).
- [14] R.A. Ahmed, A.M. Fekry, R.A. Farghali, A study of calcium carbonate/multiwalled-carbon nanotubes/chitosan composite coatings on Ti-6Al-4V alloy for orthopedic implants, *Appl. Surf. Sci.* 285 (2013) 309–316.

- [15] R.A. Ahmed, A comparative study on the corrosion performance of Ni47Ti49Co4 and Ni51Ti49 shape memory alloys in simulated saliva solution for dental applications, *Acta Metall. Sin. (Engl. Lett.)* 29 (11) (2016) 1001–1010.
- [16] R.A. Ahmed, Electrochemical properties of Ni47Ti49Co4 shape memory alloy in artificial urine for urological implant, *Ind. Eng. Chem. Res.* 54 (34) (2015) 8397–8404.
- [17] W. Sun, A.W.-Y. Tan, A. Bhowmik, F. Xue, I. Marinescu, E. Liu, Evaluation of cold sprayed graphene nanoplates-Inconel 718 composite coatings, *Surf. Coat. Technol.* 378 (2019), 125065.
- [18] F.S.d. Silva, N. Cinca, S. Dosta, I.G. Cano, M. Couto, J.M. Guilemany, A. V. Benedetti, Corrosion behavior of WC-Co coatings deposited by cold gas spray onto AA 7075-T6, *Corros. Sci.* 136 (2018) 231–243.
- [19] A.M. Fekry, R.A. Ahmed, S.A. Bioumy, Silver nanoparticle/graphene oxide/chitosan coatings for protection of surfaces in food processing, *J. Bio-Tribos-Corros.* 6 (2020) 4.
- [20] S.A. Bioumy, R.A. Ahmed, A.M. Fekry, Electrochemical corrosion behavior of graphene oxide/chitosan/silver nanoparticle composite coating on stainless steel utensils in aqueous media, *J. Bio-Tribos-Corros.* 6 (2020) 3.
- [21] G. Shen, L. Zhang, Z. Gu, Z. Zheng, Y. Liu, G. Tan, X. Jie, Zinc aluminum-layered double hydroxide(LDH)-graphene oxide(go) lubricating and corrosion-resistant composite coating on the surface of magnesium alloy, *Surf. Coat. Technol.* 437 (2022) 128354.
- [22] K.S. Jyotheender, C. Srivastava, Ni-graphene oxide composite coatings: optimum graphene oxide for enhanced corrosion resistance, *Compos. Part B* 175 (2019).
- [23] M.Y. R, C. Srivastava, Microstructure and corrosion properties of zinc-graphene oxide composite coatings, *Corros. Sci.* 152 (2019) 234–248.
- [24] J. Hu, M. Gan, L. Ma, J. Zhang, S. Xie, F. Xu, J.Z.X. Shen, H. Yin, Preparation and enhanced properties of polyaniline/grafted intercalated ZnAl-LDH nanocomposites, *Appl. Surf. Sci.* 328 (2015) 325–334.
- [25] M. Shao, F. Ning, Y. Zhao, J. Zhao, M. Wei, D.G. Evans, X. Duan, Core-shell layered double hydroxide microspheres with tunable interior architecture for supercapacitors, *Chem. Mater.* 24 (6) (2012) 1192–1197.
- [26] H. Wang, X. Xiang, F. Li, Hybrid ZnAl-LDH/CNTs nanocomposites: noncovalent assembly and enhanced photodegradation performance, *AIChE J.* 56 (2009) 768–778. NA-NA.
- [27] L. Wu, X. Ding, Z. Zheng, Y. Ma, A. Atrens, X. Chen, Z. Xie, D. Sun, F. Pan, Fabrication and characterization of an actively protective Mg-Al LDHS/Al2O3 composite coating on magnesium alloy AZ31, *Appl. Surf. Sci.* 487 (2019) 558–568.
- [28] H. Wu, L. Zhang, Y. Zhang, S. Long, X. Jie, Corrosion behavior of Mg-Al LDH film in-situ assembled with graphene on mg alloy pre-sprayed al layer, *J. Alloys Compd.* 834 (2020).
- [29] L. Yan, M. Zhou, X. Pang, K. Gao, One-step in situ synthesis of reduced graphene oxide/Zn-Al layered double hydroxide film for enhanced corrosion protection of magnesium alloys, *Langmuir* 35 (19) (2019) 6312–6320.
- [30] Y. Song, Y. Tang, L. Fang, F. Wu, X. Zeng, J. Hu, S.F. Zhang, B. Jiang, H. Luo, Enhancement of corrosion resistance of AZ31 Mg alloys by one-step in situ synthesis of ZnAl-LDH films intercalated with organic anions (ASP, La), *J. Magnes. Alloys* 9 (2) (2021) 658–667.
- [31] L. Wu, J. Wu, Z. Zhang, C. Zhang, Y. Zhang, A. Tang, L. Li, G. Zhang, Z. Zheng, A. Atrens, F. Pan, Corrosion resistance of fatty acid and fluoroalkylsilane-modified hydrophobic Mg-Al LDH films on anodized magnesium alloy, *Appl. Surf. Sci.* 487 (2019) 569–580.
- [32] X. Zheng, X. Han, X. Zhao, J. Qi, Q. Ma, K. Tao, L. Han, Construction of Ni-Co-Mn layered double hydroxide nanoflakes assembled hollow nanocages from bimetallic imidazolate frameworks for supercapacitors, *Mater. Res. Bull.* 106 (2018) 243–249.
- [33] X. Ge, C. Gu, Z. Yin, X. Wang, J. Tu, J. Li, Periodic stacking of 2D charged sheets: self-assembled superlattice of Ni-Al layered double hydroxide (LDH) and reduced graphene oxide, *Nano Energy* 20 (2016) 185–193.
- [34] D. Yu, S. Wen, J. Yang, J. Wang, Y. Chen, J. Luo, Y. Wu, RGO modified ZnAl-LDH as epoxy nanostructure filler: a novel synthetic approach to anticorrosive waterborne coating, *Surf. Coat. Technol.* 326 (2017) 207–215.
- [35] Y. Jiang, Y. Song, Y. Li, W. Tian, Z. Pan, P. Yang, Y. Li, Q. Gu, L. Hu, Charge transfer in ultrafine LDH nanosheets/graphene interface with superior capacitive energy storage performance, *ACS Appl. Mater. Interfaces* 9 (43) (2017) 37645–37654.
- [36] H. Wu, L. Zhang, C. Liu, Y. Mai, Y. Zhang, X. Jie, Deposition of Zn-G/Al composite coating with excellent cathodic protection on low-carbon steel by low-pressure cold spraying, *J. Alloys Compd.* 821 (2020).
- [37] L. Zhang, G. Hou, W. Zhai, Q. Ai, J. Feng, L. Zhang, P. Si, L. Ci, Aluminum/graphene composites with enhanced heat-dissipation properties by in-situ reduction of graphene oxide on aluminum particles, *J. Alloys Compd.* 748 (2018) 854–860.
- [38] P. John, K.B. Perdew, Matthias Ernzerhof, Generalized gradient approximation made simple, *Phys. Rev. Lett.* 77 (1996) 3865.
- [39] G.K. Joubert, From ultrasoft pseudopotentials to the projector augmented-wave method, *Phys. Rev. B* 59 (1999) 1758.
- [40] S. Grimme, J. Antony, S. Ehrlich, H. Krieg, A consistent and accurate ab initio parametrization of density functional dispersion correction (DFT-D) for the 94 elements H-Pu, *J. Chem. Phys.* 132 (15) (2010), 154104.
- [41] H.J. Monkhorst, J.D. Pack, Special points for brillouin-zone integrations, *Phys. Rev. B* 13 (12) (1976) 5188–5192.
- [42] J. Ni, J. Xue, J. Shen, G. He, H. Chen, Fabrication of ZnAl mixed metal-oxides/RGO nanohybrid composites with enhanced photocatalytic activity under visible light, *Appl. Surf. Sci.* 441 (2018) 599–606.
- [43] Y. Dong, C. Lin, S. Gao, N. Manoranjan, W. Li, W. Fang, J. Jin, Single-layered GO/LDH hybrid nanoporous membranes with improved stability for salt and organic molecules rejection, *J. Membr. Sci.* 607 (2020).
- [44] L. Wu, B. Peng, Q. Li, Q. Wang, X. Yan, K. Li, Q. Lin, Effects of Cu²⁺ incorporation on ZnAl-layered double hydroxide, *New J. Chem.* 44 (14) (2020) 5293–5302.
- [45] X. Luo, S. Yuan, X. Pan, C. Zhang, S. Du, Y. Liu, Synthesis and enhanced corrosion protection performance of reduced graphene oxide nanosheet/ZnAl layered double hydroxide composite films by hydrothermal continuous flow method, *ACS Appl. Mater. Interfaces* 9 (21) (2017) 18263–18275.
- [46] Y. Cao, D. Zheng, X. Li, J. Lin, C. Wang, S. Dong, C. Lin, Enhanced corrosion resistance of superhydrophobic layered double hydroxide films with long-term stability on Al substrate, *ACS Appl. Mater. Interfaces* 10 (17) (2018) 15150–15162.
- [47] X. Feng, Z. Yu, R. Long, X. Li, L. Shao, H. Zeng, G. Zeng, Y. Zuo, Self-assembling 2D/2D (MXene/LDH) materials achieve ultra-high adsorption of heavy metals Ni²⁺ through terminal group modification, *Sep. Purif. Technol.* 253 (2020).
- [48] M. Zhou, L. Yan, H. Ling, Y. Diao, X. Pang, Y. Wang, K. Gao, Design and fabrication of enhanced corrosion resistance Zn-Al layered double hydroxides films based anion-exchange mechanism on magnesium alloys, *Appl. Surf. Sci.* 404 (2017) 246–253.
- [49] H. Wu, G. Shen, R. Li, L. Zhang, X. Jie, G. Liu, Influence of embedded reduced graphene oxide on the corrosion-wear performance of cold sprayed Zn-RGO/Al coating in NaCl solution, *Surf. Coat. Technol.* 429 (2022).
- [50] H. Wu, G. Shen, R. Li, B. Chen, L. Zhang, X. Jie, G. Liu, The growth behavior and properties of orientated LDH film composited with reduced graphene oxide, *Surf. Coat. Technol.* 436 (2022).
- [51] H. Bai, Y. Xu, L. Zhao, C. Li, G. Shi, Non-covalent functionalization of graphene sheets by sulfonated polyaniline, *Chem. Commun. (Camb.)* 13 (2009) 1667–1669.
- [52] G. Zhang, L. Wu, A. Tang, Y. Ma, G.-L. Song, D. Zheng, B. Jiang, A. Atrens, F. Pan, Active corrosion protection by a smart coating based on a MgAl-layered double hydroxide on a cerium-modified plasma electrolytic oxidation coating on Mg alloy AZ31, *Corros. Sci.* 139 (2018) 370–382.
- [53] Z. Zhang, Z. Hua, J. Lang, Y. Song, Q. Zhang, Q. Han, H. Fan, M. Gao, X. Li, J. Yang, Eco-friendly nanostructured Zn-Al layered double hydroxide photocatalysts with enhanced photocatalytic activity, *CrystEngComm* 21 (31) (2019) 4607–4619.
- [54] F. Zhang, Z.-G. Liu, R.-C. Zeng, S.-Q. Li, H.-Z. Cui, L. Song, E.-H. Han, Corrosion resistance of Mg-Al-LDH coating on magnesium alloy AZ31, *Surf. Coat. Technol.* 258 (2014) 1152–1158.
- [55] C. Ding, Y. Tai, D. Wang, L. Tan, J. Fu, Superhydrophobic composite coating with active corrosion resistance for AZ31B magnesium alloy protection, *Chem. Eng. J.* 357 (2019) 518–532.
- [56] L. Wu, D. Yang, G. Zhang, Z. Zhang, S. Zhang, A. Tang, F. Pan, Fabrication and characterization of Mg-M layered double hydroxide films on anodized magnesium alloy AZ31, *Appl. Surf. Sci.* 431 (2018) 177–186.
- [57] L. Zhang, S. Yang, X. Lv, X. Jie, Wear and corrosion resistance of cold-sprayed Cu-based composite coatings on magnesium substrate, *J. Therm. Spray Technol.* 28 (6) (2019) 1212–1224.
- [58] S.-I.P. Woo-Jin Lee, Effects of hydroxide ion addition on anodic dissolution of pure aluminum in chloride ion-containing solution, *Electrochim. Acta* 44 (1999) 4041–4049.
- [59] A.J. Vreugdenhil, V.J. Gelling, M.E. Woods, J.R. Schmelz, B.P. Enderson, The role of crosslinkers in epoxy–amine crosslinked silicon sol–gel barrier protection coatings, *Thin Solid Films* 517 (2) (2008) 538–543.
- [60] J. Chen, Y. Song, D. Shan, E.-H. Han, In situ growth of Mg-Al hydrotalcite conversion film on AZ31 magnesium alloy, *Corros. Sci.* 53 (10) (2011) 3281–3288.
- [61] J.H. Chu, L.B. Tong, M. Wen, Z.H. Jiang, K.S. Wang, H.J. Zhang, Graphene oxide film as a protective barrier for Mg alloy: worse or better is dependent on a chemical reduction process, *Carbon* 145 (2019) 389–400.
- [62] F. Wu, J. Liang, Z. Peng, B. Liu, Electrochemical deposition and characterization of Zn-Al layered double hydroxides (LDHs) films on magnesium alloy, *Appl. Surf. Sci.* 313 (2014) 834–840.
- [63] H. Yan, J. Wang, C. Meng, X. Wang, S. Song, X. Fan, L. Zhang, H. Li, W. Li, M. Zhu, Towards long-term corrosion and wear protection of Al alloy: synergy of Ti3C2Tx flake and micro-arc oxidation coating, *Corros. Sci.* 174 (2020).
- [64] X. Fan, H. Yan, M. Cai, S. Song, Y. Huang, M. Zhu, Achieving parallelly-arranged Ti3C2Tx in epoxy coating for anti-corrosive/wear high-efficiency protection, *Compos. Part B* 231 (2022).
- [65] Q. Wang, D. O'Hare, Recent advances in the synthesis and application of layered double hydroxide (LDH) nanosheets, *Chem. Rev.* 112 (7) (2012) 4124–4155.
- [66] X. Xu, D. Liu, X. Zhang, C. Liu, D. Liu, W. Zhang, Influence of ultrasonic rolling on surface integrity and corrosion fatigue behavior of 7B50-T7751 aluminum alloy, *Int. J. Fatigue* 125 (2019) 237–248.
- [67] L. Calabrese, P. Bruzzaniti, E. Proverbio, Pitting corrosion of aluminum alloys in anhydrous ethanol, *Mater. Corros.* 69 (12) (2018) 1815–1826.
- [68] W. Xu, J. Liu, Microstructure and pitting corrosion of friction stir welded joints in 2219-O aluminum alloy thick plate, *Corros. Sci.* 51 (11) (2009) 2743–2751.